

to appear in *Astrophysical Journal*

Formation of Disk Galaxies: Feedback and the Angular Momentum problem

Jesper Sommer-Larsen, Sergio Gelato and Henrik Vedel¹

Theoretical Astrophysics Center, Juliane Maries Vej 30, DK-2100 Copenhagen Ø, Denmark

ABSTRACT

When only cooling processes are included, smoothed-particle hydrodynamical simulations of galaxy formation in a Cold Dark Matter hierarchical clustering scenario consistently produce collapsed objects that are deficient in angular momentum by a factor of about 25 relative to the disks of observed spiral galaxies. It is widely hoped that proper allowance for star formation feedback effects will resolve this discrepancy. We explore and compare the effects of including two different types of feedback event: uniform reheating of the entire Universe to 5×10^5 K at a redshift $z \sim 6$, and gas blow-out from pregalactic gas clouds comparable to present-day dwarf galaxies at a somewhat lower redshift. We find that blow-out is far more successful than early reheating, and that it may even be sufficient to solve the angular momentum problem. We see indications that the remaining angular momentum deficit (a factor of 5 in the blow-out models) is due to current limitations in the numerical method (SPH) used in our and other authors' work. Our most successful models distinguish themselves by the fact that a large fraction of the gas is accreted very gradually, in a cooling flow from a surrounding hot phase, rather than by mergers of massive cold clumps.

Subject headings: cosmology: theory — dark matter — galaxies: evolution — galaxies: formation — galaxies: structure — methods: numerical

¹Current Address: Dansk Meteorologisk Institut, Lyngbyvej 100, DK-2100 Copenhagen Ø, Denmark

1. Introduction

The formation of galactic disks is one of the most important unsolved problems in astrophysics today. In the currently favored hierarchical clustering framework, disks form in the potential wells of dark matter halos as the baryonic material cools and collapses dissipatively. It has been shown (Fall & Efstathiou 1980, hereafter FE80) that disks formed in this way can be expected to possess the observed amount of angular momentum (and therefore the observed spatial extent for a given mass and profile shape), but only on condition that the infalling gas retain most of its original angular momentum.

Numerical simulations of this collapse scenario in a cosmological context (e.g., Navarro & Benz 1991, Navarro & White 1994, Navarro, Frenk, & White 1995), however, have so far consistently indicated that when only cooling processes are included the infalling gas loses too much angular momentum (by over an order of magnitude) and the resulting disks are accordingly much smaller than required by the observations. This discrepancy is known as the *angular momentum problem* of galaxy formation. It arises from the fact that gas cooling is very efficient at early times, leading to the rapid condensation of gas clouds which are then promptly slowed down by dynamical friction against the surrounding dark matter halo before they eventually merge to form the central disk. A mechanism is therefore needed that prevents, or at least delays, the collapse of protogalactic gas clouds and allows the gas to preserve a larger fraction of its angular momentum as it settles into the disk. (Such a mechanism is also helpful in solving the *overcooling problem*, namely the observation (White & Rees 1978) that cooling is expected to be so efficient at early times that most of the gas should have been converted to stars well before the assembly of present-day galactic disks.) Weil, Eke, & Efstathiou (1998, hereafter WEE98) have shown that if the cooling is suppressed (by whatever means), numerical simulations can indeed yield more realistically sized disks. The physical mechanism by which cooling is suppressed or counteracted, however, is still uncertain.

An early candidate was the extragalactic ionizing ultraviolet and soft X-ray (UVX) background which is thought to permeate the Universe at least at redshifts $z \lesssim 3-4$ (with quasars as an important source) and maybe considerably earlier. Such a field provides a natural explanation of the observed low optical depth in neutral hydrogen (Gunn & Peterson 1965, Efstathiou 1992) and of the properties of the Lyman α forest (Hernquist et al. 1996). The effect of such a field on galaxy formation was explored by Vedel, Hellsten, & Sommer-Larsen (1994, hereafter VHSL94). These authors concluded that the UVX background does indeed affect the formation of both small and large galaxies. However, the UVX background is not in itself sufficient to solve the angular momentum problem: it is better at inhibiting the accretion of low-density gas at low redshift than the formation of

high-density clouds at high redshift (when inverse Compton cooling is particularly efficient and capable of counteracting the UVX heating, even if one assumes that the UVX field is already strong at that time). This has been pointed out among others by Navarro & Steinmetz (1997, hereafter NS97), who even find that the UVX field exacerbates the angular momentum deficit. (This last detail is at variance with the result of VHSL94. The broader fact that the UVX field alone does not solve the angular momentum problem, however, is much less controversial.)

A different heating mechanism is therefore required. In this paper we explore and compare two candidate mechanisms: uniform reheating of the entire Universe at $z \sim 6$ (as could have been caused by energy feedback from a pregalactic phase of star formation), and more conventional, localized feedback in the form of gas blow-out by supernova explosions in the first generation of collapsed subgalactic objects at a somewhat later epoch. We also compare the results to those of purely passive cooling simulations, with no heat sources other than the UVX background.

We begin (in section 2) with some plausibility arguments and estimates of relevant physical parameters for our two reheating scenarios. In particular, we derive (§ 2.1) an upper bound on the reheating temperature in the first scenario. Section 3 briefly presents the numerical methods used, namely the numerical code and the model parameters and initial conditions. The simulations themselves are presented in section 4, and the results analyzed in section 5. We summarize our conclusions in section 6.

2. Reheating scenarios

2.1. Early reheating of the Universe

Consider the hypothesis that the Universe was reheated and reionized at a relatively high redshift z_{RH} , when it was still fairly homogeneous on galactic scales. One way in which this could have come about is if at those redshifts a fraction of the gas was had collapsed into a dense, cold phase (cf. Tegmark et al. 1997) out of which a small amount of stars formed. The more massive of these would quickly explode as supernovae, releasing enough energy to reheat the medium more or less uniformly to temperatures $T_{RH} \sim 10^5$ K, as we proceed to show.

Assuming that a fraction f_* of the gas is turned into stars, that each unit of mass in stars gives rise (over a short time scale of a few million years) to ν_{SN} type II supernovae each of which releases an energy $E_{SN} \sim 10^{51}$ erg, the energy released by supernovae per

unit mass can be written as

$$f_\star \nu_{SN} E_{SN}. \quad (1)$$

To account for radiative losses we further assume that the released energy is turned into thermal energy of the remaining ISM with some efficiency $\beta \leq 1$. One can easily show that the temperature of the remaining gas then increases to

$$T_{RH} \simeq \frac{2}{3} \frac{\mu m_p}{k_B} \nu_{SN} E_{SN} \frac{\beta f_\star}{1 - (1 - R)f_\star} \simeq 2.4 \times 10^5 \beta \nu_{100} E_{51} \left(\frac{f_\star}{0.01} \right) \text{ K}, \quad (2)$$

where μ is the molecular weight (which we take to be 0.6), m_p is the mass of the proton, k_B is Boltzmann’s constant, R is the stellar return fraction ($0 \leq R \lesssim 0.4$ for “standard” initial mass functions), $\nu_{100} = (100 M_\odot) \nu_{SN}$, and $E_{SN} = 10^{51} E_{51}$ erg. In the last part of equation (2) we have assumed $(1 - R)f_\star \ll 1$.

We now give two reasons why f_\star must be small, resulting in an upper limit on T_{RH} . First, most of the stars that form at z_{RH} and are responsible for reheating the gas out of which disk galaxies later condense are expected to end up in the halos of these same galaxies (cf. Sommer-Larsen et al. 1997); as the mass of the stellar halo of the Milky Way is only about 1% of the total baryonic mass, $f_\star \lesssim 0.01/(1 - R)$. For a Scalo (1986) “best fit” initial mass function (IMF), $\nu_{100} \sim 0.4$. So with $E_{51} \simeq 1$ one would expect, from equation (2), that $T_{RH} \lesssim 10^5$ K. There are some indications (Kennicutt, Tamblyn & Congdon 1994, Sommer-Larsen 1996, Tsujimoto et al. 1997) that the global IMF is more top-heavy than Scalo’s, implying $\nu_{100} \sim 1$. Using this, and setting $\beta = 1$, a firm upper limit to T_{RH} is $T_{RH} \lesssim 5 \times 10^5$ K. Note, however, that if the early IMF was extremely top-heavy (and consequently $(1 - R) \ll 1$) the Milky Way stellar halo mass argument given above could be bypassed and one could in principle have $f_\star \gg 0.01$ and $T_{RH} > 5 \times 10^5$ K.

The second, stronger argument is based on chemical evolution considerations, in particular the fact that oxygen is ejected only by type II supernovae ($M \gtrsim 8 M_\odot$). Beers & Sommer-Larsen (1995) found that the disk of the Milky Way extends down to very low metallicities: $[Fe/H] \lesssim -2$, or equivalently $[O/H] \lesssim -1.5$ as $[O/Fe] \simeq 0.5$ in Galactic metal-poor stars. Let M_O be the mass of oxygen produced and ejected by a type II supernova. Its value is fairly insensitive to the IMF: $M_O \simeq 2.0 M_\odot$ for a Scalo IMF and $\simeq 2.6 M_\odot$ for a Salpeter IMF (cf. Pagel 1997). These numbers are consistent with the observationally inferred value for SN 1987A. The oxygen abundance is then given by:

$$Z_i(O) = \frac{f_\star}{1 - (1 - R)f_\star} \nu_{SN} M_O \simeq f_\star \nu_{SN} M_O, \quad (3)$$

where again we have made use of $(1 - R)f_\star \ll 1$ in the last part of equation (3). It then

follows that

$$f_\star \simeq \frac{Z_i(O)}{\nu_{SN} M_O} = 0.016 \left(\frac{Z_i(O)}{10^{-1.5} Z_\odot(O)} \right) \nu_{100}^{-1} \left(\frac{M_O}{2M_\odot} \right)^{-1}. \quad (4)$$

Inserting this into equation (2) yields

$$T_{RH} \simeq \frac{2\beta\mu m_p E_{SN} Z_i(O)}{3 k_B M_O} = 3.8 \times 10^5 \beta E_{51} \left(\frac{Z_i(O)}{10^{-1.5} Z_\odot(O)} \right) \left(\frac{M_O}{2M_\odot} \right)^{-1} \text{ K}, \quad (5)$$

for $\mu = 0.6$ and $Z_\odot(O) = 0.01$ (e.g., Pagel 1997). This expression does not depend on the values of ν_{SN} and R , so it is a considerably more robust estimate of T_{RH} than what is obtained with the Galactic stellar halo argument above. The existence of a very metal-weak tail of the Galactic disk has been questioned (Ryan & Lambert 1995, Chiba & Yoshii 1997), but there are other indications that the typical abundance produced by a (hypothetical) early phase of star formation (“population III”) is very low. In Lyman α clouds with neutral hydrogen column density $N(HI)$ as low as $10^{14.5} \text{ cm}^{-2}$, carbon is detected but at a low level: $[C/H] \sim -2.5$ (Songaila & Cowie 1996, Lu, Sargent, & Barlow 1997). With $[C/O] \simeq -0.5$, as detected in metal-weak stars as well as in metal-weak extragalactic H II regions (e.g., Pagel 1997), this corresponds to $[O/H] \sim -2$, similar to what is obtained from the metal-weak thick disk tail argument above. There are even indications (Ostriker & Gnedin 1996, Gnedin & Ostriker 1997, Lu et al. 1998) that population III enrichment is at least 1.5 dex lower than this.

At very high redshifts inverse Compton cooling dominates. The cooling rate is given by (Ikeuchi & Ostriker 1986)

$$\Lambda_C = 5.41 \times 10^{-36} n_e T (1+z)^4 \text{ erg s}^{-1} \text{ cm}^{-3}, \quad (6)$$

where n_e is the number density of free electrons in units of cm^{-3} . For a fully ionized, primordial plasma the inverse Compton cooling timescale is given by

$$t_C = \frac{\mathcal{E}}{\dot{\mathcal{E}}_C} = \frac{3n_e k_B T}{(X+1)\mu\Lambda_C} \simeq 10^9 \left(\frac{7}{1+z} \right)^4 \text{ yr} \quad (7)$$

which is independent of density and temperature. (X is the Hydrogen mass fraction; we assume $X = 0.76$ in our numerical estimates.) For an $\Omega = 1$, $H_0 = 50 \text{ km s}^{-1}$ cosmology t_C is comparable to the Hubble time at $z = z_{eq} \simeq 7$. For $z_{RH} \gtrsim z_{eq}$ reheating is therefore ineffective. We consequently choose $z_{RH} < z_{eq}$.

2.2. Gas blow-out from pregalactic clouds

An alternative to this diffuse reheating scenario is to assume that larger condensations do form early on, but that star formation activity is strong enough to expel the gas from

these regions before they merge into larger objects (Dekel & Silk 1986). The gas then needs to cool and condense again, now more slowly and gradually since the mean density is lower. The most significant change is that the disk grows in a gentle cooling flow from a dilute, hot ($T \sim 10^6$ K) corona rather than through mergers of inspiralling high-density clumps. The primary feedback process is supernova explosions, but stellar winds and UV radiation from massive stars also contribute to reheating the interstellar medium (Hellsten 1995).

In this scenario, reheating occurs in a more patchy manner and radiative cooling is the main competing effect. Unfortunately the balance between heating and cooling is very difficult to establish from first principles, since it depends strongly on the manner in which the energy from the stars is deposited into the ISM. Supernovae are thought to be largely responsible for maintaining the multiphase structure of the ISM. This is an area of ongoing research, and best discussed in a separate paper. Sommer-Larsen, Hellsten & Vedel (1999) use a simplified treatment of the ISM as a two-phase medium composed of a warm ($T \sim 10^4$ K) and a hot ($T \sim 10^6$ K) phase to show that supernova-driven hot gas outflows can be very efficient during the early stages of galaxy formation when the metallicity of the gas is low.

To illustrate why the multiphase structure of the ISM cannot be ignored for a proper treatment, let us consider a schematic model similar to that used by various authors (e.g., Katz 1992, Navarro & White 1993, Mihos & Hernquist 1994) to represent star formation and feedback in numerical simulations of galaxy formation. Let the star-formation rate in a dense gas cloud be given by

$$\frac{dM_\star}{dt} = \frac{M_{gas}}{t_\star}, \quad (8)$$

where $t_\star = \tau t_{ff}$, $t_{ff} = (4\pi G \rho_{gas})^{-1/2}$, and $\tau \geq 1$ is an inverse star-formation efficiency parameter. The rate of SN explosion energy input into the inter-stellar medium (ISM) is then given by

$$\dot{E}_{heat} = \frac{dM_\star}{dt} \nu_{SN} E_{SN}, \quad (9)$$

in which ν_{SN} and E_{SN} are defined as in equation (2). The rate of radiative cooling per unit volume is written in terms of the *cooling function* $\Lambda_{cool}(T)$ as

$$\dot{\mathcal{E}}_{cool} = \Lambda_{cool}(T) n_H^2. \quad (10)$$

It is straightforward to show that the ratio of the rate of SN energy input to the rate of cooling in the gas cloud is

$$q \equiv \frac{\dot{E}_{heat}}{\dot{\mathcal{E}}_{cool}} = \frac{\nu_{SN} E_{SN} (4\pi G)^{1/2} m_p^{3/2}}{\tau \Lambda_{cool}(T) n_H^{1/2} X^{3/2}} = 1.5 \frac{\nu_{100} E_{51}}{\tau \Lambda_{-23} n_H^{1/2}}, \quad (11)$$

where $\nu_{100} = (100M_{\odot})\nu_{SN}$, $E_{SN} = 10^{51}E_{51}$ erg, $\Lambda = 10^{-23}\Lambda_{-23}$ erg cm $^{-3}$ s $^{-1}$), and n_H is the hydrogen number density in units of cm $^{-3}$.

The balance q between the rates of heating and cooling depends fairly sensitively on the mean effective density n_H of the gas. Katz (1992) found in his simulations that if the gas is treated as a single-phase medium (of relatively high mean density in the star-forming regions) that is heated more or less uniformly by feedback processes, then $q \ll 1$ and the heat is quickly radiated away, resulting in no appreciable blow-out. On the other hand, if the supernova energy is unevenly distributed and predominantly serves to heat a low-density gas phase, then it can only be radiated away over a much longer time scale, and the effect of multiple supernova explosions can be additive.

Other mechanisms for local reheating have been proposed. For example, the radiation from a quasar located in the host protogalaxy could heat the surrounding gas. However, one can show that photoionization cannot raise the gas temperature above $T_{QH} \lesssim 10^5$ K for any reasonable choice of quasar spectrum (Hellsten, private communication). Compton heating has been discussed by Krolik, McKee, & Tarter (1981). It might be important relatively close ($d \lesssim 10$ kpc) to the quasar. More important, however, might be the effect of quasar winds, as discussed recently by Silk & Rees (1998). Note, however, that the comoving density of quasars peaks quite late, at $z \sim 2$; it remains to be seen whether this is early enough for the reheating to be effective.

3. The code and the initial conditions

3.1. The code

We use the gridless Lagrangian N -body and Smoothed Particle Hydrodynamics code TREESPH described in VHSL94, with only a minor change in the method by which the energy equation for the gas is solved. Our TREESPH code is modeled after that of Hernquist & Katz (1989).

We include gas cooling and heating terms as in VHSL94. The heating corresponds to a redshift-dependent, homogeneous and isotropic UVX background field. We assume a rather hard (spectral index -1) field

$$J_{\nu}(z) = J_{-21}(z) \times 10^{-21} \left(\frac{\nu}{\nu_L} \right)^{-1} \text{ erg cm}^{-2} \text{ sr}^{-1} \text{ Hz}^{-1} \text{ s}^{-1}, \quad (12)$$

where ν_L is the Lyman limit frequency, with the redshift-dependent normalization

$$J_{-21}(z) = \frac{10}{1 + [5/(1+z)]^4} \quad (13)$$

of Efstathiou (1992). For greater realism one could build on the detailed study of Haardt & Madau (1996), but our adopted background field is quantitatively not too dissimilar from theirs (once allowance is made for our simplified spectral shape), at least at redshifts $z \lesssim 3$, and should be adequate for the level of detail we can represent in the simulations. The code also incorporates inverse Compton cooling (equation [6]), which is also explicitly redshift-dependent.

Due to the impossibility of properly representing the multiphase structure of the ISM in an SPH simulation at the level of resolution we can afford to run and to the lack of a clear physical basis (or even of a reliable empirical calibration) for schemes such as the kinetic energy feedback term of Navarro & White (1993), we do not attempt to follow star formation and feedback in the manner pioneered by Katz (1992). Instead, we mimic feedback events occurring at well-defined epochs by instantaneously altering the state of the gas at that time, then continuing the simulation. This is adequate for our present purpose, which is to gain a qualitative insight into the effect of varying the epoch and manner of reheating rather than to pursue the much more ambitious and long-term goal of a fully realistic simulation.

The simulations use artificial viscosity parameters $\alpha_v = 0.9$, $\beta_v = 2\alpha_v$. The smoothing length of each SPH particle is adjusted so as to keep the number of neighbors close to 50.

3.2. The initial conditions

Our initial conditions are based on a standard ($\Omega = 1$, $\Lambda = 0$) Cold Dark Matter (CDM) model with Hubble constant $H_0 = 100h \text{ km s}^{-1} \text{ Mpc}^{-1} = 50 \text{ km s}^{-1} \text{ Mpc}^{-1}$. On the scales of interest to us the effective index of the power spectrum is approximately -2 : $P(k) \propto k^{-2}$. Following Eke, Cole, & Frenk (1996) we normalize the spectrum to $\sigma_8(z = 0) = 0.5$, where as customary σ_8^2 is the mass variance within spheres of comoving radius $8h^{-1} \text{ Mpc}$, extrapolated from the linear regime of perturbation growth.

We begin by performing a large-scale simulation within a sphere of comoving radius 40 Mpc. Individual halos are then selected from the final state and individually sampled at higher resolution. The original large-scale simulation is used to provide a tidal field acting on the resampled halos, which are evolved individually in a second round of simulations.

Approximately 2.5×10^5 particles are initially placed on a cubic lattice within that

sphere. Position and velocity perturbations are then applied according to the Zel’dovich (1970) approximation. The perturbations consist of the superposition of $N_k \sim 4 \times 10^4$ plane waves sampling a Gaussian random field with variance given by the power spectrum. Following Navarro & White (1994) we use an equal number of waves per logarithmic interval in k -space. The phases of these waves are random and only wavenumbers between the fundamental and Nyquist wavenumber of the lattice are included. The initial redshift (which determines the amplitude of the initial perturbations) is $z_i \simeq 18$.

The evolution of this system to $z = 0$ is then computed using a tree code. Only gravitational forces are included in this first simulation. In the final state we identify four virialized, isolated halos with circular velocities between 200 and 260 km s^{-1} in the innermost 20 Mpc of the simulation. We expect that a significant fraction of such halos should host disk galaxies similar to the Milky Way since the circular velocities are in the same range and our halos were chosen to lie “in the field”, away from larger concentrations of mass. We adopt the customary working definition of the virial radius as the radius r_{200} of a sphere enclosing a mean density of 200 times the critical cosmic value. Tracing the particles in these halos back to the initial conditions, we find that they all come from regions that fit within spheres of comoving radius ~ 3 Mpc.

Each of these spheres at $z \simeq 18$ is then resampled with a lattice 4 times finer in each spatial dimension. Each sphere contains about 7000 points of this new lattice. We assign one dark matter (DM) particle and two SPH particles to each of these points. The SPH particles are positioned at random within one gas gravitational softening length of their parent DM particle. Note that at this redshift the DM particles are spaced by about 14 kpc, so that each SPH particle is rather closely associated with its parent DM particle. Table 1 lists the precise number of SPH and DM particles in each sphere. We adopt a baryonic mass fraction $\Omega_b = 0.05$, consistent with nucleosynthesis constraints ($0.01h^{-2} \lesssim \Omega_b \lesssim 0.02h^{-2}$). This leads to masses of $1.1 \times 10^9 M_\odot$ for the DM and $2.9 \times 10^7 M_\odot$ for the SPH particles. The SPH particles are assigned an initial thermal energy corresponding to a temperature $T_i \simeq 100$ K. In order to include small-scale power that could not be sampled in the first simulation, we add shorter-wavelength plane waves in a way that preserves an equal number of waves per interval in $\log k$.

We use stored intermediate results from the large cosmological simulation to provide a time-dependent tidal field acting on the resampled spheres. This is achieved by treating the original particles outside the resampled sphere as passive, interpolating their positions between successive snapshots of the original simulation and incorporating them into the particle tree that the code constructs on each step for the evaluation of gravitational forces. Gravitational interactions between particles are softened according to the prescription of

Hernquist & Katz (1989), with softening lengths 3 kpc for the gas particles, 10 kpc for the dark matter particles, and 40 kpc for the “passive” dark matter particles that provide the tidal field from the original large-scale simulation. The gravitational softening lengths are kept constant in physical units throughout the evolution of the system.

4. The simulations

We carry out three sets of four simulations each. In what follows, the symbols $S1$, $S2$, $S3$, and $S4$ correspond to the four high-resolution spheres, and the subscripts PA , RH , and BO to the three sets of simulations. These subscripts stand respectively for “passive”, “reheating”, and “blow-out”.

In the PA simulations, no stellar feedback is applied to the thermal history of the gas. The only non-adiabatic effects present (aside from the usual shock-capturing artificial viscosity) are radiative and inverse Compton cooling, and heating through photoionization by the background UVX field. These simulations are meant to extend the results of VHSL94 to more realistic initial conditions than the uniform top-hat these authors used, as well as to provide a basis for assessing the effectiveness of our reheating experiments.

In the RH simulations, the gas is reheated wholesale to a temperature of 5×10^5 K at a redshift $z = 6$. (We have also performed a test simulation in which this reheating occurs at $z = 18$ rather than $z = 6$, and found as expected that the heat was dissipated very quickly by inverse Compton cooling. The final result was essentially indistinguishable from that of the corresponding “passive” simulation.) Apart from this instantaneous reheating event, the system is evolved passively, exactly as in the PA runs.

In the BO simulations, all cold ($T < 3 \times 10^4$ K), relatively dense ($n_H > 10^{-3.5} \text{cm}^{-3}$) gas clumps are identified in the simulation at $z = 2.4$ and their particles instantaneously redistributed uniformly within spherical shells between radii $r_{\text{in}} = \alpha r_0$ and $r_{\text{out}} = 2\alpha r_0$ around the center of mass of each clump. In other words, the gas is blown out but not blown away from the systems. Here $r_0 \sim 50$ kpc is the virial radius of the largest progenitor halo to the final object at that redshift ($z = 2.4$), and α a tuning factor of order unity. The results we present here were obtained with $\alpha = 1.2$, but tests we have performed suggest that the results are not very sensitive to the precise value of this parameter. For robustness r_0 is not measured directly from the state of the simulation at $z = 2.4$ but estimated from V_{200} for the final halos (at $z = 0$) using the isothermal sphere approximation (cf. Mo, Mao, & White 1998)

$$r_0 = \frac{V_{200}}{10H(z)} = 400 \left(\frac{V_{200}}{200 \text{ km s}^{-1}} \right) (1+z)^{-3/2} \text{ kpc}, \quad (14)$$

where $H(z)$ is the Hubble parameter at redshift z and the last part of equation (14) follows from our choice of cosmology. The temperature of the “blown out” gas was not changed and, for a given gas cloud, all the “blown out” gas was given the same velocity, the center of mass velocity of the parent gas cloud. This was done to ensure that no extra angular momentum or thermal energy was added to the simulations (the angular momenta of the original cold gas clouds were insignificant). As in the *RH* case, no form of feedback is applied apart from this instantaneous event. The redshift $z = 2.4$ is appropriate in our case because our simulations at that time contain a number of gas clumps of the requisite size (namely the largest size of object for which blow-out can reasonably be expected to be significant), and these are about to merge into larger structures. The picture in our simulations presents a striking resemblance to the Hubble Space Telescope observation by Pascarelle et al. (1996) of a group of small galaxies at that same redshift, apparently in the process of merging into a larger object. In a more realistic implementation (which may well be required if one were to do such simulations at higher resolution) the blow-out would occur continuously rather than at a single point in time as in the schematic model we study here. Note that our choice of redshift is tied to the formation history of the galaxies we are studying, and might therefore be sensitive to the choice of cosmological model and to the mass of the final halo.

5. Results

5.1. Disk masses, sizes, angular momenta

Table 2 (which is closely modeled after Table 1 of NS97) presents some global properties of the final collapsed objects in our twelve simulations. The first column is the simulation label, as described in the previous section. Columns 2, 3, and 4 respectively hold the virial mass M_{200} , the virial radius r_{200} , and the circular velocity V_{200} at the virial radius. The numbers N_{gas} and N_{DM} of gas and DM particles inside the virial radius are in columns 5 and 6, and the corresponding masses M_{gas} and M_{DM} in columns 7 and 8. Columns 9, 10, and 11 show the number of gas particles N_{disk} , the corresponding baryonic mass M_{disk} , and the ratio $M_{\text{disk}}/\Omega_b M_{200}$ for the cold disk present at the end of each simulation. We define this disk as consisting of all cold ($T < 3 \times 10^4$ K) gas particles within $r_{\text{max}} = 10$ kpc from the (iteratively determined) center of mass of the disk. The results remain virtually unchanged if we adopt $r_{\text{max}} = 5$ kpc instead. For the *BO* models we used r_{max} values of 20 and 10 kpc, respectively, since it turns out that larger disks can form in these models.

In all the simulations, only about 40–60% of the gas mass inside the virial radius has cooled and settled into the disk; this low fraction is largely due to the presence of the UVX

field (VHSL94, NS97). We find no systematic trend in cooled mass fraction between the three sets of simulations. For a given set of initial conditions, the final virial mass M_{200} is very nearly the same for all three runs. The gas mass M_{gas} fluctuates a little more, but without exhibiting any clear systematic trend. The scatter in the cooled central disk gas mass is larger still, but (perhaps remarkably) does not exhibit any clear systematic trend either; a much larger number of realizations would probably be needed if we wanted to find a dependence.

How large are the cold disks, and how much angular momentum do they contain? We need to answer this question both for the simulation results and for real galaxies. For the latter we start from existing catalogues by Mathewson, Ford, & Buchhorn (1992) and by Byun (1992). The full catalogues are diameter-limited, but one of us (JSL) has carefully extracted a subsample of 203 late-type (Sb–Sd) galaxies in such a way as to compensate for the selection bias of the full dataset. We use as a measure of the linear sizes of the observed disks their inclination-corrected I -band exponential disk scale lengths b_I^0 . For consistency with the numerical simulations we assume $h = 0.5$ in converting from redshifts to linear distances. It turns out that for our sample $b_I^0 \propto V_c^\eta$ (with some scatter), where V_c is the amplitude of the flat part of the rotation curve and $\eta \simeq 1$. We cannot directly measure the specific angular momenta of these disks, but we can estimate them from the relation

$$j = 1.68bV_c, \quad (15)$$

which holds exactly for a purely exponential disk truncated at $R_t = 4b$ with a perfectly flat rotation curve and no bulge contribution. The radial cutoff corresponds to the observation by van der Kruit & Searle (1982) that the disks of spiral galaxies have an edge at that radius. It follows from $b \propto V_c^\eta$ that $j \propto V_c^{1+\eta}$. In much of the rest of this paper, we express results in terms of a normalized specific angular momentum $\tilde{j} \equiv j/V_c^2$.

For the simulations, it is easier to determine j directly (since we have full knowledge of the particle distribution in phase space), but in many cases harder to assign an exponential scale length b due to resolution limitations. We tentatively estimate b as $\langle R^2 \rangle^{1/2}/1.94$, which again holds exactly for a perfect exponential disk truncated at $R_t = 4b$. (Here $\langle R^2 \rangle$ is the mass-weighted average of the square of the cylindrical radius R .) We measure V_c at $R = 30$ kpc, where the rotation curves turn out to be approximately flat. The values of V_c and b are tabulated respectively in columns 2 and 3 of table 3.

In figure 1 we plot the exponential disk scale length b as a function of circular speed V_c , both for our simulation results (filled triangles represent the *PA* runs, squares the *RH* runs, circles the *BO* runs) and for the observational data. One can clearly see from this figure that the simulated disks are far too centrally concentrated for their circular speed. The situation is particularly bad for the passive simulations (whose scale lengths b are too small

by an order of magnitude); by contrast, one of the blow-out runs is almost acceptable. The early reheating runs are intermediate.

Figure 2 shows the relation between j and b for the simulations. (The values of j are listed in column 5 of table 3.) It is closer to quadratic ($j \propto b^2$) than linear. Sommer-Larsen, Vedel, & Hellsten (1998) interpret this as a consequence of the gravitational softening length being comparable to or larger than the extent of the disk. This indicates that the problem is actually even worse than figure 1 would imply, since the values of b from the simulations are artificially inflated as an effect of gravitational softening.

In figure 3 we plot the values of j/V_c^2 versus V_c for the simulations. The solid horizontal line corresponds to the mean from the observational data set, with dotted and dashed lines corresponding to one and two standard deviations from this mean. For the passive simulations, the angular momentum deficit is highly significant, and amounts to a factor of about 25. This amount is broadly consistent with the findings of NS97. (Navarro, Frenk, & White (1995) found a smaller factor of about 5, but as discussed in NS97 this is probably due to resolution problems. The simulations we present here have nearly the same resolution as those of NS97.) Our “reheating” and “blow-out” simulations clearly reduce the gap with the observations; the blow-out models are particularly encouraging. The deficit for the latter is only about a factor 5, which can perhaps be accounted for by limitations in the numerical method. A detailed examination of the results of WEE98 (see especially their figures 1c and 14) reveals that their stellar disks also lie below the observations by a similar factor. We are inclined to agree with them in considering this a success.

Besides the values of V_c , b_{disk} , and j_{disk} already mentioned, table 3 lists our computed values for the dimensionless spin parameter $\lambda \equiv J|E|^{1/2}/GM^{5/2}$ (column 4) evaluated at the *infall radius* r_{inf} (column 6). This radius is defined by $M_{\text{DM}}(r_{\text{inf}})/(1 - \Omega_b) = M_{\text{disk}}/\Omega_b$, and is of order 100 kpc in all our runs. It represents the characteristic radius, at the present time, of the dark matter originally associated with the amount of gas currently in the disk. Evaluating λ at r_{200} does not significantly affect the results. The spin parameters for our halos are consistent with the theoretical prediction of a broad distribution around $\lambda \sim 0.05$ (Barnes & Efstathiou 1987, Heavens & Peacock 1988). The angular momentum deficit in our disks is therefore unlikely to be due to our having chosen an unrepresentative set of parent halos.

The azimuthally averaged disk surface density profiles are shown in figure 4 for the *BO* runs. The disks are close to exponential over a reasonable range of radii (out to at least 4 kpc), with scale lengths of order 1–2 kpc. Figure 5 shows the rotation curves, recomputed from the particle distribution at $z = 0$ under the assumption of negligible gravitational softening, for the same four runs. Consistent with our previous observation that the angular

momentum deficit has been reduced but not completely eliminated, there is still a hint of an excessive central concentration of mass in some of the runs, but the general behavior appears reasonably realistic otherwise.

The most extended disk found in our simulations is that of $S4_{BO}$. We show an edge-on view in figure 6, and a face-on view (with arrows to represent the velocity field) in figure 7. This disk extends beyond 10 kpc and exhibits a distinct warp in the outer regions. A spiral arm may even be discerned in the face-on view.

5.2. Analysis of the infall process

We distinguish between a “cold” ($T < 3 \times 10^4$ K) and a “hot” ($T > 3 \times 10^4$ K) gas phase. In practice most of the “hot” gas in our simulations is much hotter ($T \sim 10^6$ K) than our demarcation threshold, due to cooling times being short at intermediate temperatures and densities. The cold gas is in a rather dense state ($n_H \gtrsim 10^{-3} \text{ cm}^{-3}$), while the hot gas is more dilute.

We measure the amount of gas that has been accreted onto the central disk during each of the intervals $[t_i, t_i + \Delta t_i]$ between successive snapshots in our simulations. For the runs presented in this work the snapshots are evenly spaced with $\Delta t_i = 1$ Gyr. The accreted material is classified as “hot” or “cold” according to its state at t_i . A quantity of interest is the fraction f_{hot} of the total disk mass that was in the form of hot gas just before being accreted onto the existing cold disk. In figure 8 we plot the specific angular momenta $\tilde{j}_{\text{disk}} \equiv j_{\text{disk}}/V_c^2$ of the disks in the final state of our simulations against f_{hot} . As one could have expected given the presence of an UVX background, f_{hot} is rather large for all our simulations ($f_{\text{hot}} \gtrsim 0.5$). The simulations with reheating tend to have even higher values $f_{\text{hot}} > 0.75$, reflecting the fact that the formation of cold clumps is suppressed at early times. While there is a clear trend in that on average the *BO* runs have both larger f_{hot} and larger \tilde{j}_{disk} than the *RH* runs, and the *RH* runs than the *PA* runs, the scatter in \tilde{j}_{disk} vs. f_{hot} in each group of simulations is quite large. Within each group there appears to be no correlation between \tilde{j}_{disk} and f_{hot} . This reminds us that factors other than the thermodynamic state (density and temperature) of the accreted material play a role in determining the angular momentum of the disk.

Let us examine the history of angular momentum acquisition. In each time bin $[t_i, t_i + \Delta t_i]$ we compute the angular momentum of both the infalling material ($\vec{j}_{\text{inf},i} = j_{\text{inf},i} \vec{e}_{\text{inf},i}$, where the \vec{e} 's are unit vectors) and the preexisting disk (the unit vector of which at time t_i will be written $\vec{e}_{\text{disk},i}$). In figure 9 we plot the average $\langle \vec{e}_{\text{disk},i} \cdot \vec{e}_{\text{inf},i} \rangle$ over

all time bins i for which data are available. The results are insensitive to whether only the hot gas (filled symbols) or all the accreted gas (open symbols) is used in determining \vec{e}_{inf} . As expected, the final angular momentum is larger in disks that have more coherent infall. Interestingly, the *BO* runs appear to possess this property of experiencing coherent infall to a larger degree than the other sets of runs. The reason, we believe, is that much of the infalling material is material that has been “blown out” of a clump at some earlier time and retains the imprint of the orbital motion of its parent clump. In the *PA* runs, the same material would be accreted in a single event and cause an abrupt change in the angular momentum of the disk. In the *BO* runs, it is accreted over a longer period and thus \vec{e}_{disk} already includes part of the realignment.

Figure 10 shows the distribution of specific angular momenta \tilde{j}_{disk} as a function of the dispersion $\sigma_{\vec{e}_{\text{inf}}}$ in the angular momentum orientation of the infalling material. This dispersion is defined by

$$\sigma_{\vec{e}_{\text{inf}}}^2 = \langle (\vec{e}_{\text{inf},i} - \langle \vec{e}_{\text{inf},i} \rangle)^2 \rangle, \quad (16)$$

with both means being taken over the time bins i , and measures the scatter in the orientation of \vec{e}_{inf} . A perfectly isotropic distribution of \vec{e}_{inf} would result in $\sigma_{\vec{e}_{\text{inf}}} = 1$. This confirms the trend that the final angular momentum is reduced when the infall is disordered.

In two of the *PA* runs, the central object undergoes a major merger of cold gas, defined as an event in which the mass ΔM_{cold} of cold gas gained during the last Gyr is at least 30% of the current disk mass M . These runs are the ones that possess the smallest specific angular momenta. We plot the peak values of $\Delta M_{\text{cold}}/M$ obtained during the evolution of each of our simulated systems in figure 11. The solid line on this plot shows the result of a linear least-squares fit, and confirms the visual impression that there is a (negative) correlation between major cold merger events and the final angular momentum of the disk.

Figure 12 shows \tilde{j}_{disk} versus the normalized total specific angular momentum of the infalling gas, $\tilde{j}_{\text{inf}} = j_{\text{inf}}/V_c^2$, defined by

$$j_{\text{inf}} = \frac{|\vec{J}_{\text{disk}}(t_{i_0}) + \sum_{i \geq i_0} \vec{J}_{\text{inf}}(t_i)|}{M_{\text{disk}}(z=0)}. \quad (17)$$

If no angular momentum were lost or gained by the disk other than by accretion, we would expect j_{disk} to equal j_{inf} . This is not the case. The difference indicates that a significant part of the angular momentum is lost either during the last ~ 0.5 Gyr before accretion or at the time of accretion. This happens even when almost all the gas is accreted as hot and dilute: the dependence of the angular momentum loss on the type (*PA*, *RH*, or *BO*) of model is much weaker than what we found in figure 3 for \tilde{j}_{disk} . We suspect that this late loss of angular momentum is due to numerical transport effects as the SPH particles get

incorporated into the disk. If so, this contribution to the angular momentum loss (a factor of about 4) is unlikely to have a physical counterpart. We should therefore consider our deficit of a factor of 5 in \tilde{j}_{disk} for the *BO* simulations (figure 3), and the similar result of WEE98, as a success in that no further unknown physical processes seem to be required. If instead of \tilde{j}_{disk} (as in figure 3) we plot \tilde{j}_{inf} (figure 13), the agreement in disk angular momentum between the simulated and observed systems becomes quite satisfactory for all of the *BO* runs and even for some *RH* and *PA* runs.

One may wonder whether the large differences in j_{inf} between runs started from the same initial conditions is due to their somehow having accreted different material. To the extent that there are differences in the final disk masses M_{disk} (table 2), this must clearly be the case; but as we have seen, the variation in M_{disk} does not show any discernible systematic trend. Since most of the angular momentum is imparted by tidal torques in the course of the simulations, it is not very instructive to compute the initial angular momentum of the gas that ends up in the disk. Instead, we evaluate the analogue of j_{inf} for the dark matter initially associated with this gas, and ask whether this new quantity

$$j_{\text{inf,DM}} \equiv \frac{|\vec{J}_{\text{disk,DM}}(t_{i_0}) + \sum_{i \geq i_0} \vec{J}_{\text{inf,DM}}(t_i)|}{M_{\text{disk,DM}}(z = 0)} \quad (18)$$

is in any way correlated with j_{inf} . We plot \tilde{j}_{inf} against $\tilde{j}_{\text{inf,DM}}$ in figure 14. We find no evidence of a correlation. The same can be said of \tilde{j}_{disk} versus $\tilde{j}_{\text{inf,DM}}$ in figure 15.

The connection between j_{inf} and $j_{\text{inf,DM}}$ may of course have been washed out by angular momentum exchange between the DM particles in the halo, as well as by the divergence of orbits between DM and gas particles that were initially associated with each other. It is therefore equally instructive to compare \tilde{j}_{inf} to the dimensionless spin parameter λ of the final dark matter halo, computed both within r_{200} and within the baryonic infall radius r_{inf} . We do this in figure 16, and again find no signal.

Figure 17 shows $\tilde{j}_{\text{inf,DM}}$ versus circular speed V_c . As proposed by FE80, tidal torques appear to produce just enough specific angular momentum in the dark matter halos to be consistent with observations. This, however, requires that the gas associated with the dark matter contracted dissipatively to form galactic disks with at most a minor loss of angular momentum. Figure 18 shows $\tilde{j}_{\text{inf,DM}}$ (computed for the DM associated with all infalling gas, both hot and cold) versus the spin parameter λ of the dark matter halo evaluated at the baryonic infall radius. A trend of increasing $\tilde{j}_{\text{inf,DM}}$ with increasing λ is seen, supporting the proposal by FE80 that the spin parameter of a dark matter halo is an important parameter in determining the specific angular momentum of the disk galaxy formed in its central region.

6. Conclusions

We have carried out TREESPH simulations of the formation of Milky Way-sized disk galaxies in a cosmological context. For the “passive” variant of such simulations, i.e. when the effects of stellar feedback processes are neglected, we confirm previous reports that the simulated disks are far too small (by about a factor of 10) and poor in specific angular momentum (by a factor of about 25) by comparison with observations of real galaxies. This is true even for simulations where 80% or more of the final mass of the disk is accreted from hot, dilute gas rather than mergers of cold clumps. These “passive” simulations are a natural extension of the work of VHSL94, and by using cosmological initial conditions rather than isolated uniform spheres they remove an objection raised by NS97 against that work.

Uniform reheating of all the gas in the Universe at $z \sim 6$, while reducing the angular momentum deficit to some extent, is not as effective as later blow-out of gas from a first generation of cold star-forming clouds, at least as long as the reheating temperature does not exceed 5×10^5 K, which we estimate is a firm upper limit. This estimate is based mainly on chemical enrichment constraints, but it is worth noting that with some (conservative) assumptions on the initial mass function, one can get a similar bound from the mass of our Galaxy’s stellar halo.

Instantaneous blow-out (at $z \simeq 2.4$ in our simulations), on the other hand, leads to a significant closing of the gap between observed and simulated values of the specific angular momentum. The remaining mismatch develops mostly in the late stages of gas infall and in the subsequent evolution of the disk, suggesting that it may be an artifact of artificial viscosity in the SPH method.

The success of the blow-out model appears related to the fact that the gas is accreted onto the central disk in a very gentle way, without abrupt changes of angular momentum orientation. There is no obvious difference in the angular momentum of the dark matter associated with the accreted gas between the different sets of simulations.

There is still considerable room for improvement in our ability to simulate the formation of disk galaxies. Some of it will depend on our ability to increase the numerical resolution. We have seen that the structure of the disks is affected by gravitational softening, and that much of the angular momentum is lost in the late phases of accretion. We plan to discuss this issue in detail in a future paper; for now let us point out that the test of shear-free artificial viscosity presented in NS97 is incomplete, in that it only considers the abrupt collapse of cold gas, not the steady growth of the disk in a cooling flow (which would be much more relevant to our simulations, and is also more in keeping with the widely held

view that actual galactic disks formed by gradual accumulation of material). Irregularities in the spatial arrangement of the SPH particles in the transition region from the hot to the cold phase can also contribute to angular momentum transport, and shear-free artificial viscosity formulations are more vulnerable to such small-scale disorder (in effect, the flow is more turbulent). While shear-free viscosity is undoubtedly helpful in preventing further secular evolution within an already settled disk, increased numerical resolution may be the only truly effective way of improving the solution in the transition region from the hot halo to the cold disk.

It would also be very tempting to incorporate star formation into the simulations in a more direct way, as other authors have done, by converting some of the gas mass into new “stellar” collisionless particles whose orbits are then integrated explicitly. To be consistent with observations of the stellar content of our own Galaxy, the bulk of this conversion should only occur after the gas has settled into the disk. A natural expectation is that this conversion might allow more of the angular momentum in the disk to be retained, since the stellar component is not subject to artificial viscous effects. However, the results of Steinmetz & Navarro (1998) suggest to us that this effect is not sufficiently strong to make a significant difference to the results, at least in the situation they considered (which did not include any particular mechanisms for delaying gas cooling and star formation).

We have benefited considerably from the comments of K. Gorski, U. Hellsten, C. Lacey, J. Navarro, B. Pagel, an anonymous referee, and the editor S. Shore. This work was supported by Danmarks Grundforskningsfond through its support for the establishment of the Theoretical Astrophysics Center.

REFERENCES

- Barnes, J., & Efstathiou, G. 1987, *ApJ*, 319, 575
- Beers, T. C., & Sommer-Larsen, J. 1995, *ApJS*, 96, 175
- Byun, Y. I. 1992, PhD thesis, The Australian National University
- Chiba, M., & Yoshii, Y. 1997, *ApJ*, 490, L73
- Dekel, A., & Silk, J. 1986, *ApJ*, 303, 39
- Efstathiou, G. 1992, *MNRAS*, 256, P43
- Eke, V. R., Cole, S., & Frenk, C. S. 1996, *MNRAS*, 282, 263
- Fall, S. M., & Efstathiou, G. 1980, *MNRAS*, 193, 189 (FE80)
- Gnedin, N. Y., & Ostriker, J. P. 1997, *ApJ*, 486, 581
- Gunn, J. E., & Peterson, B. A. 1965, *ApJ*, 142, 1633
- Haardt, F., & Madau, P. 1996, *ApJ*, 461, 20
- Heavens, A., & Peacock, J. 1988, *MNRAS*, 232, 339
- Hellsten, U. 1995, PhD thesis, University of Copenhagen
- Hernquist, L., & Katz, N. 1989, *ApJS*, 70, 419
- Hernquist, L., Katz, N., Weinberg, D. H., Miralda-Escudé, J. 1996, *ApJ*, 457, 51
- Ikeuchi, S., & Ostriker, J. P. 1986, *ApJ*, 301, 522
- Katz, N. 1992, *ApJ*, 391, 502
- Kennicutt, R. C., Tamblyn, P., & Congdon, C. 1994, *ApJ*, 435, 22
- Krolik, J. H., McKee, C. F., & Tarter, C. B. 1981, *ApJ*, 249, 422
- van der Kruit, P. C., & Searle, L. 1982, *A&A*, 110, 61
- Lu, L., Sargent, W. L. W., & Barlow, T. A. 1997, in *Cosmic Chemical Evolution* (IAU Symp. 187)
- Lu, L., Sargent, W. L. W., Barlow, T. A., & Rauch, M. 1998, *AJ*, submitted, astro-ph/9802189

- Mathewson, D. S., Ford, V. L., & Buchhorn, M. 1992, *ApJS*, 81, 413
- Mihos, J. C., & Hernquist, L. 1994, *ApJ*, 437, 611
- Mo, H. J., Mao, S., & White, S. D. M. 1998, *MNRAS*, 295, 319
- Navarro, J. F., & Benz, W. 1991, *ApJ*, 380, 320
- Navarro, J. F., & White, S. D. M. 1993, *MNRAS*, 265, 271
- Navarro, J. F., & White, S. D. M. 1994, *MNRAS*, 267, 401
- Navarro, J. F., Frenk, C. S., & White, S. D. M. 1995, *MNRAS*, 275, 56
- Navarro, J. F., & Steinmetz, M. 1997, *ApJ*, 478, 13 (NS97)
- Ostriker, J. P., & Gnedin, N. Y. 1996, *ApJ*, 472, L63
- Pagel, B. E. J. 1997, *Nucleosynthesis and Chemical Evolution of Galaxies*, Cambridge University Press
- Pascarelle, S. M., Windhorst, R. A., Keel, W. C., & Odewahn, S. C. 1996, *Nature*, 383, 45
- Ryan, S. G., & Lambert, D. L. 1995, *AJ*, 109, 2068
- Scalo, J. M. 1986, *Fund. Cosm. Phys.*, 11, 1
- Silk, J., & Rees, M. J. 1998, *A&A*, 331, L1
- Sommer-Larsen, J. 1996, *ApJ*, 457, 118
- Sommer-Larsen, J., Beers, T. C., Flynn, C., Wilhelm, R., & Christensen, P. R. 1997, *ApJ*, 481, 771
- Sommer-Larsen, J., Hellsten, U., & Vedel, H. 1999, in preparation
- Sommer-Larsen, J., Vedel, H., & Hellsten, U. 1998, *MNRAS*, 294, 485
- Songaila, A., & Cowie, L. L. 1996, *AJ*, 112, 335
- Steinmetz, M., & Navarro, J. F. 1998, *ApJ*, submitted (astro-ph/9808076)
- Tegmark, M., Silk, J., Rees, M. J., Blanchard, A., Abel, T., & Palla, F. 1997, *ApJ*, 474, 1
- Tsujimoto, T., Yoshii, Y., Nomoto, K., Matteucci, F., Thielemann, F., & Nashimoto, M. 1997, *ApJ*, 483, 228

- Vedel, H., Hellsten, U., & Sommer-Larsen, J. 1994, MNRAS, 271, 743 (VHSL94)
- Weil, M. L., Eke, V. R., & Efstathiou, G. 1998, MNRAS, 300, 773 (WEE98)
- White, S. D. M., & Rees, M. J. 1978, MNRAS, 183, 341
- Zel'dovich, Ya. B. 1970, A&A, 5, 84

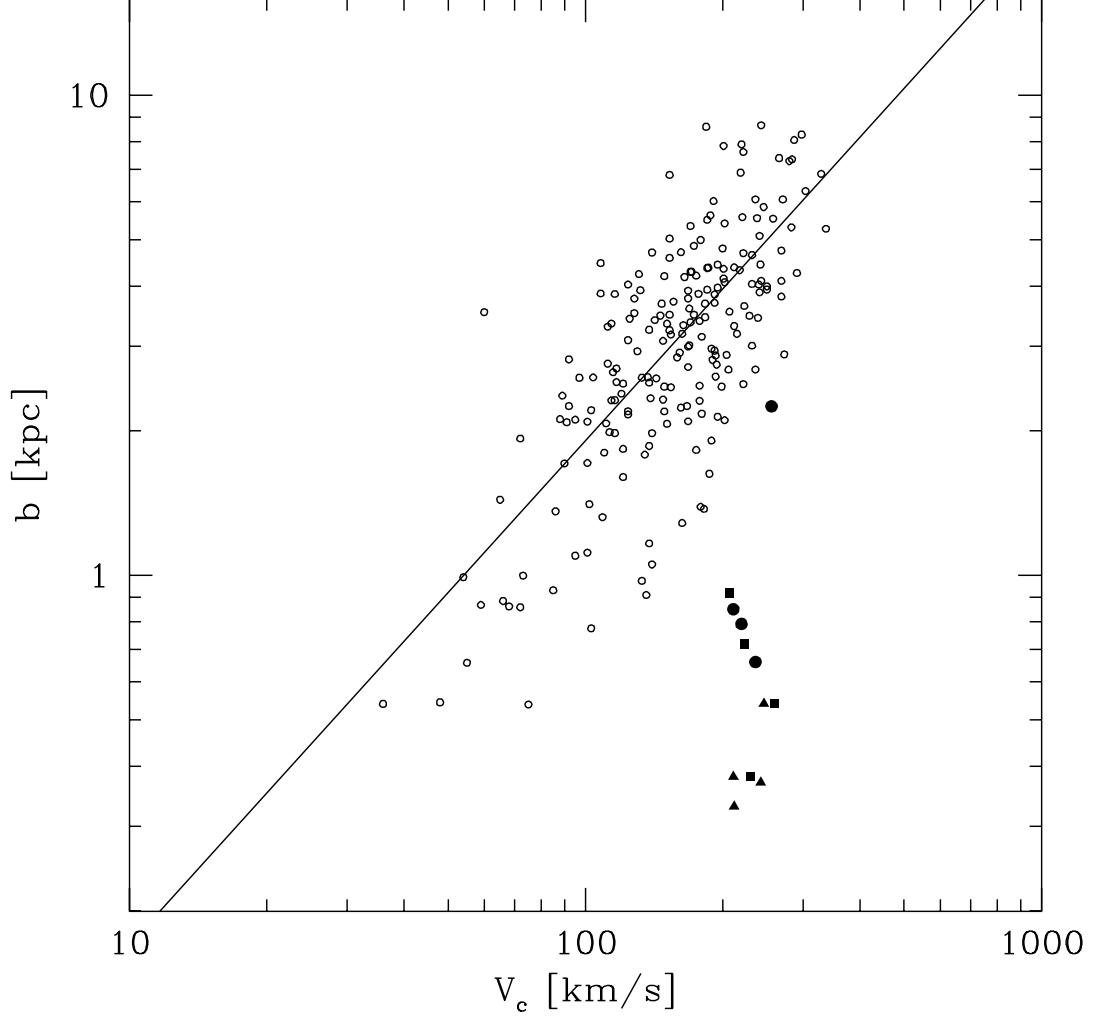


Fig. 1.— Exponential disk scale lengths b as a function of circular speed V_c for a sample of 203 Sb-Sd galaxies (open circles), and for the disks in our *PA* (“passive”, triangles), *RH* (“reheating”, squares), and *BO* (“blow-out”, circles) simulations. The solid line is a linear least-squares fit to the observational data.

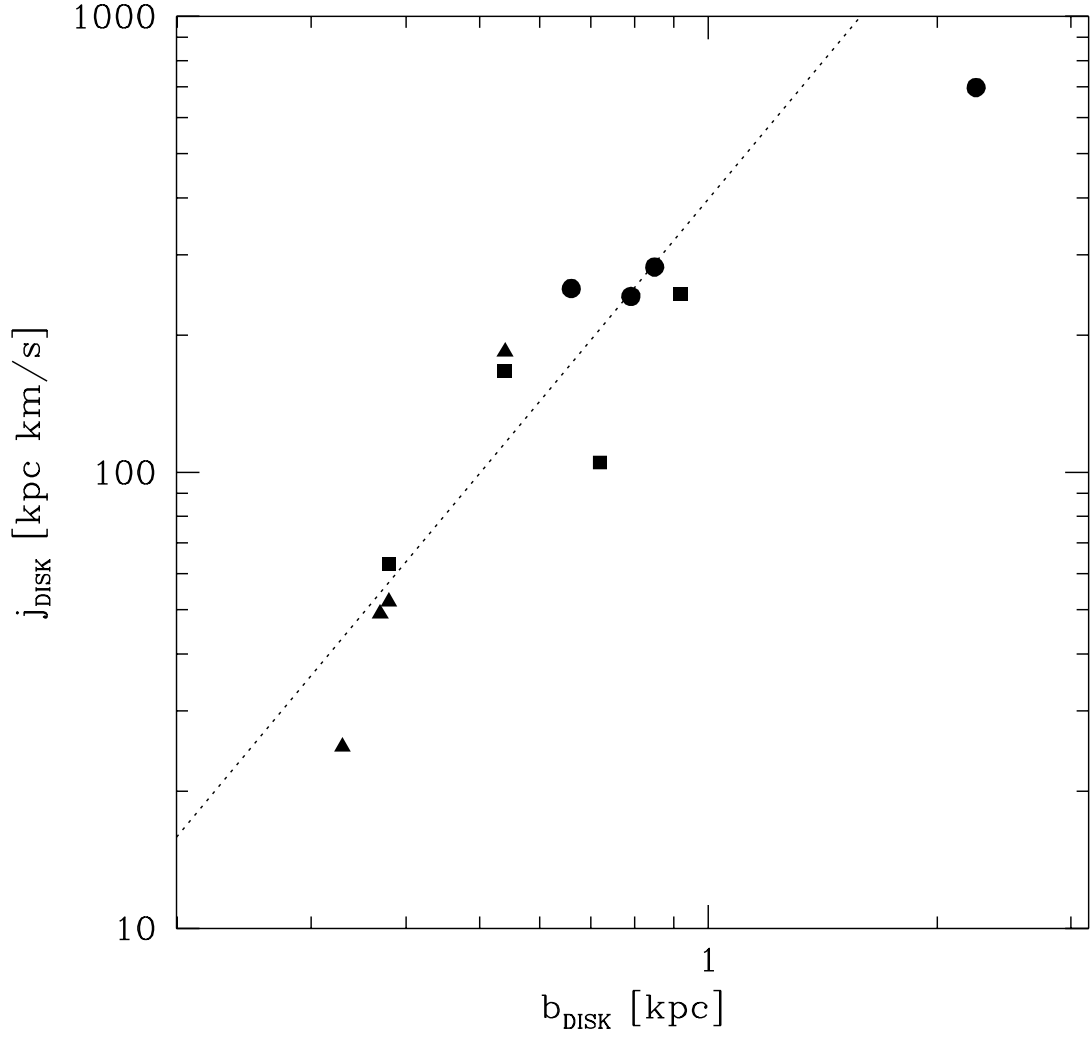


Fig. 2.— Specific angular momenta versus scale length for the simulated disks (symbols as in figure 1). The dotted line has a slope of 2, corresponding to $j_{\text{disk}} \propto b_{\text{disk}}^2$ (see text), and an arbitrary zero point.

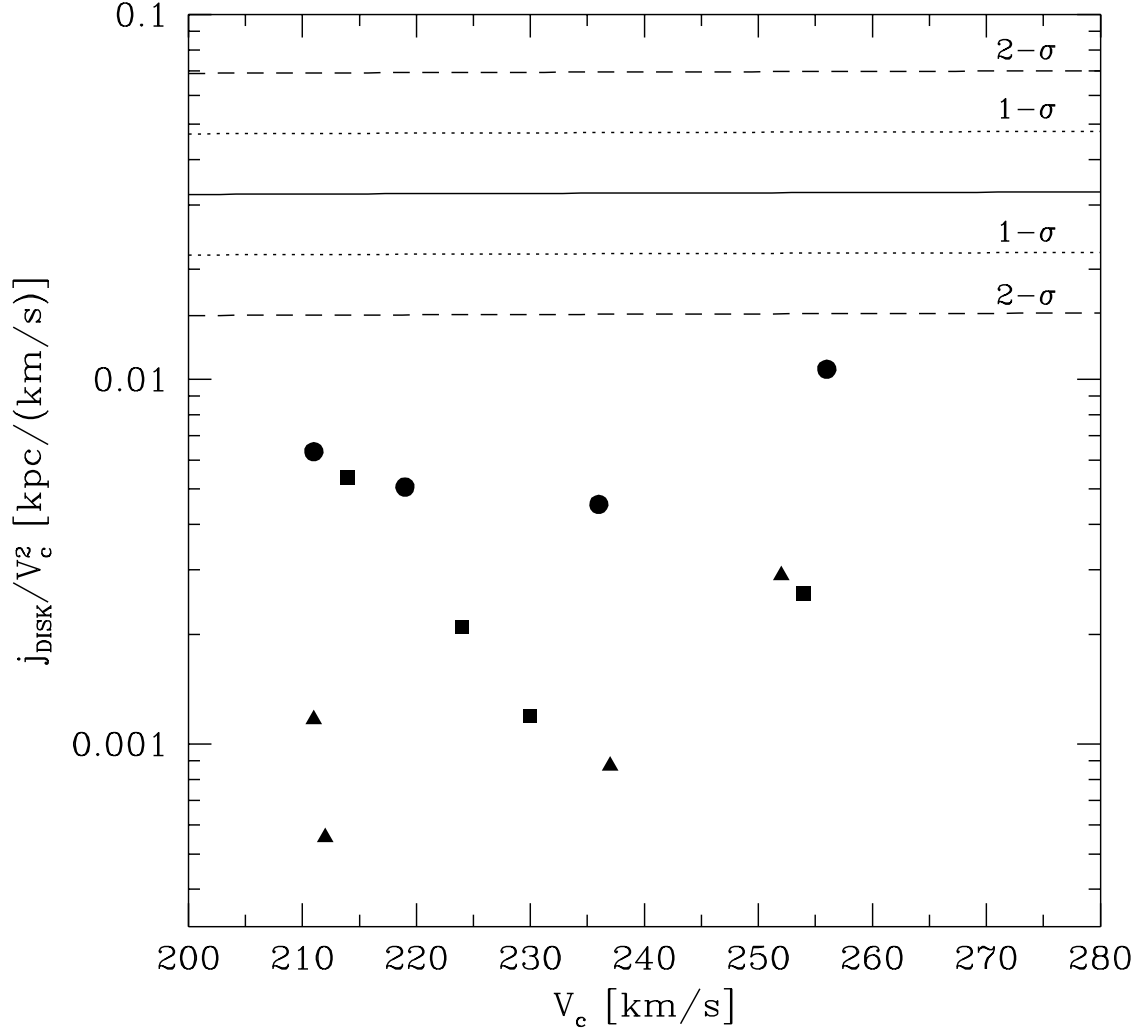


Fig. 3.— Normalized specific angular momentum $\tilde{j}_{\text{disk}} \equiv j_{\text{disk}}/V_c^2$ for the simulations (symbols as in figure 1). The solid line shows the mean value from the observational data, the dotted and dashed lines bracket the 1σ and 2σ intervals around this mean.

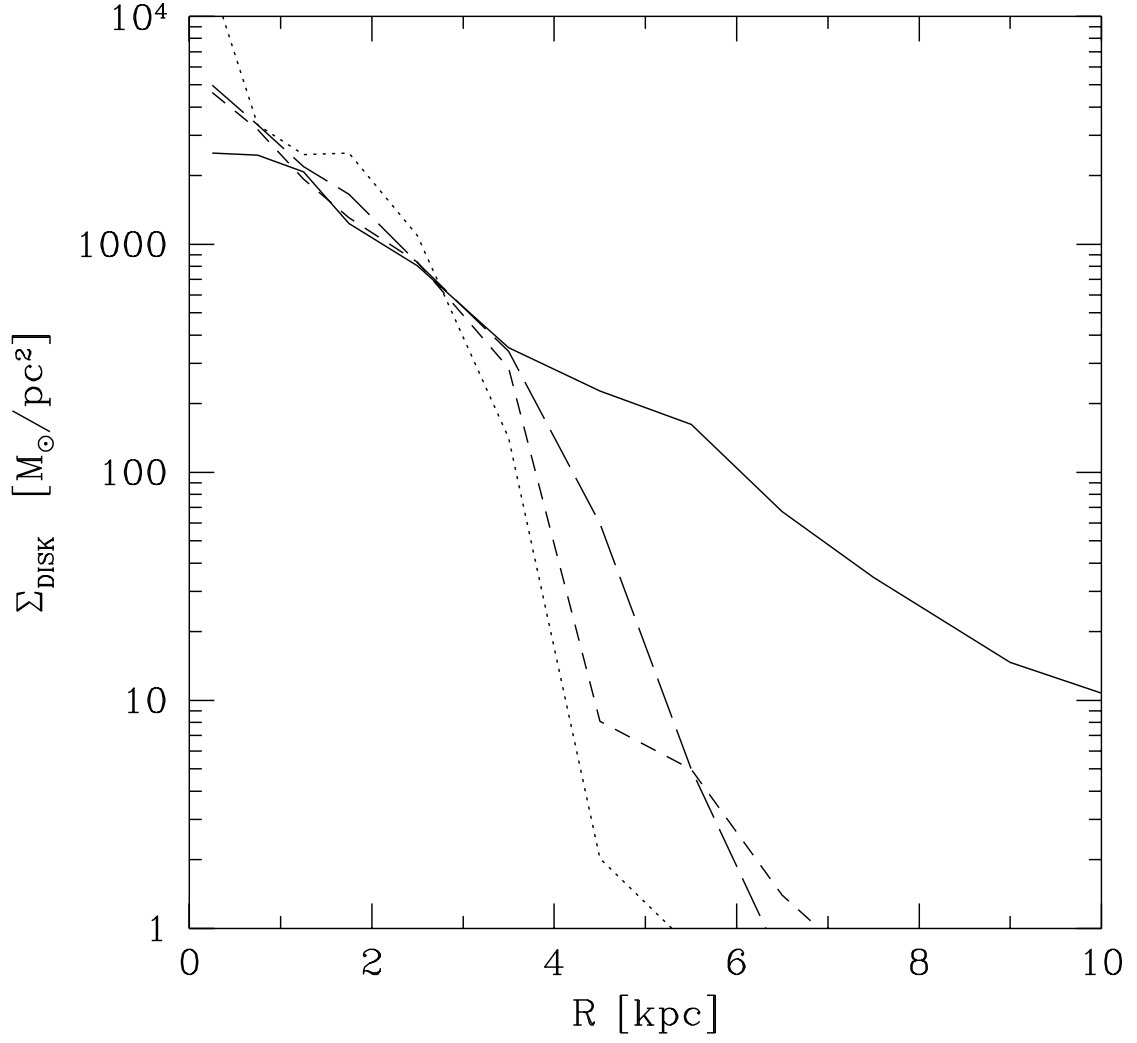


Fig. 4.— Azimuthally averaged disk surface density profiles at $z = 0$ of model galaxies $S1_{BO}$ (long-dashed line), $S2_{BO}$ (short-dashed line), $S3_{BO}$ (dotted line) and $S4_{BO}$ (solid line) from the gas “blow-out” simulations.

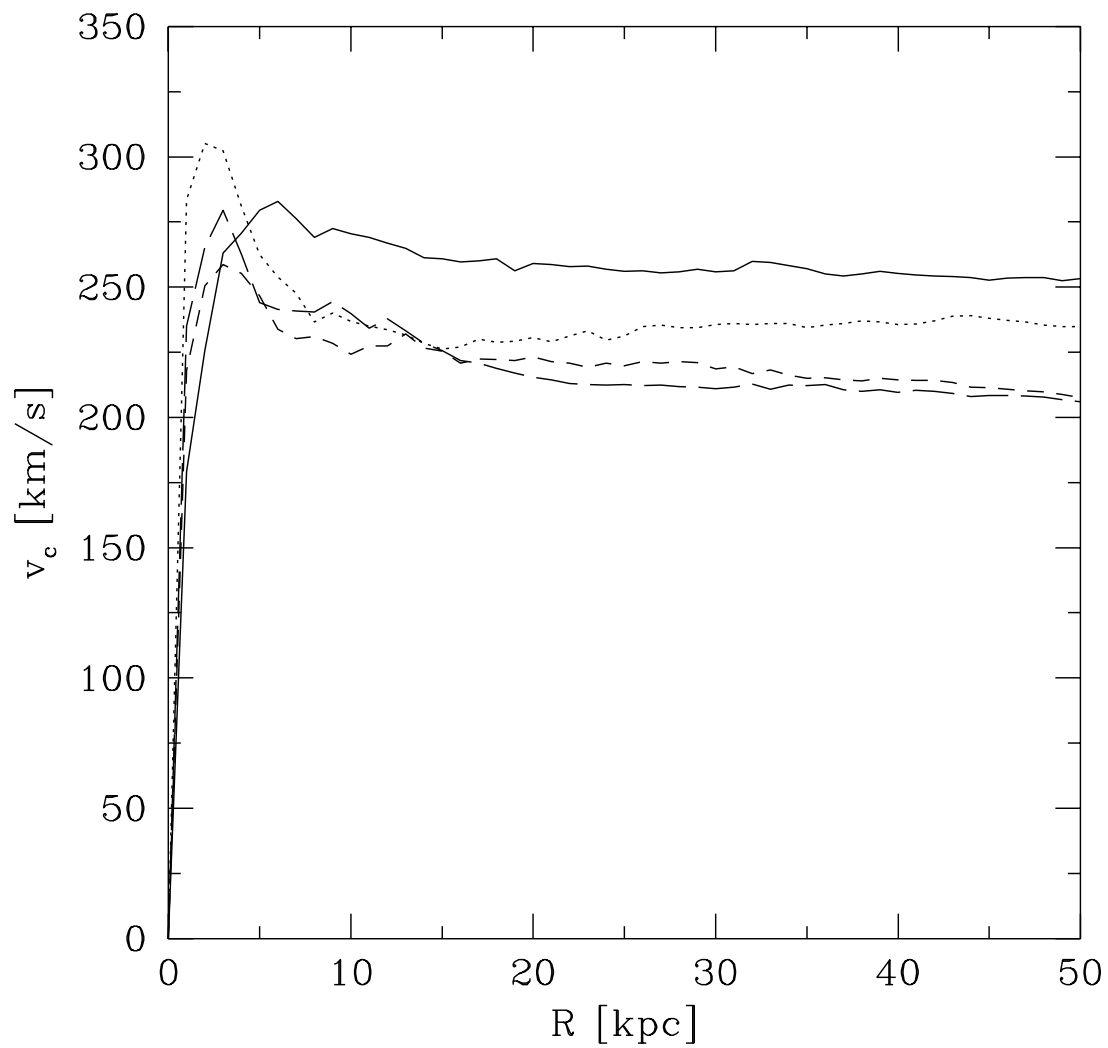


Fig. 5.— Rotation curves at $z = 0$ for the “blow-out” models. Symbols are as in figure 4.

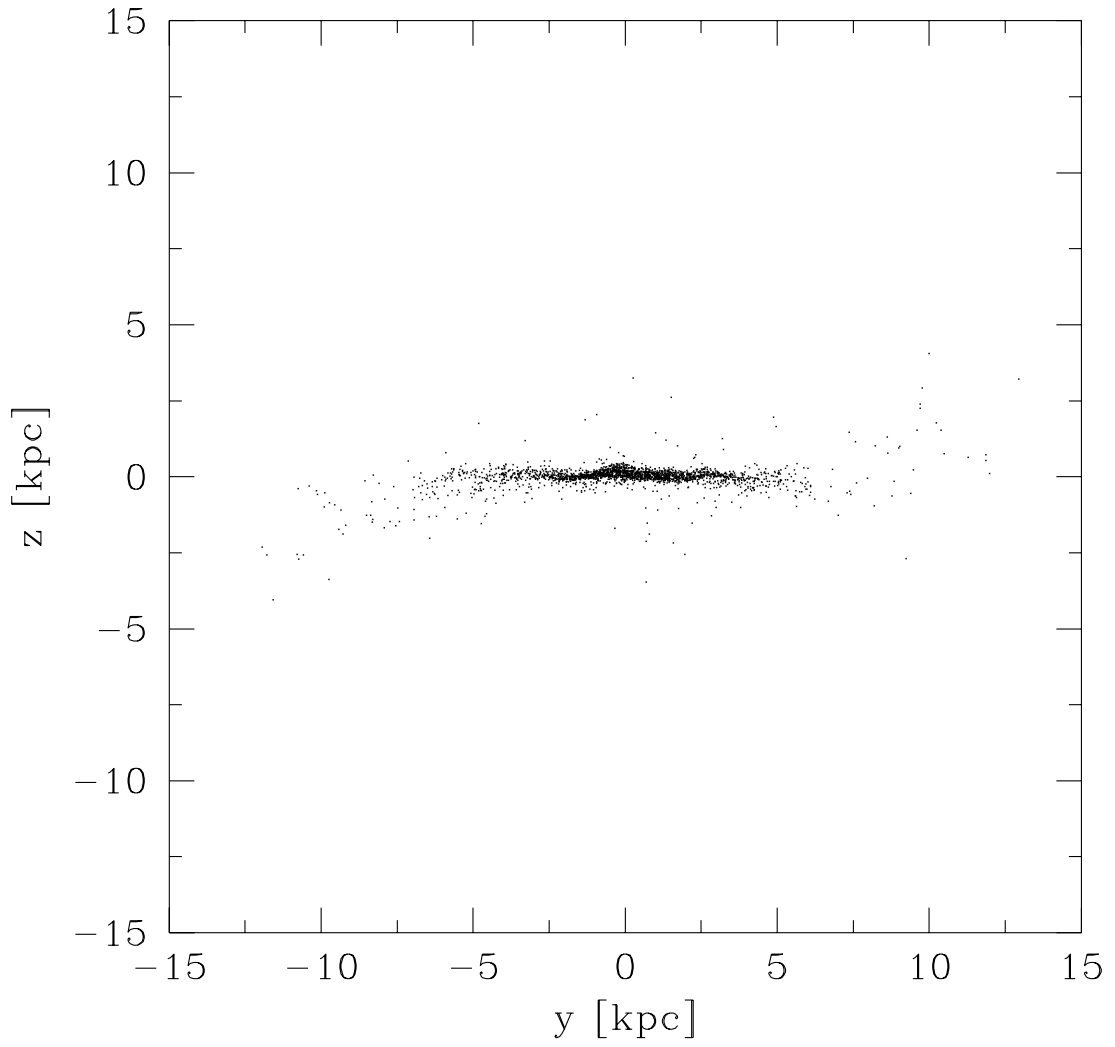


Fig. 6.— Edge-on view of model galaxy $S4_{BO}$ at $z = 0$.

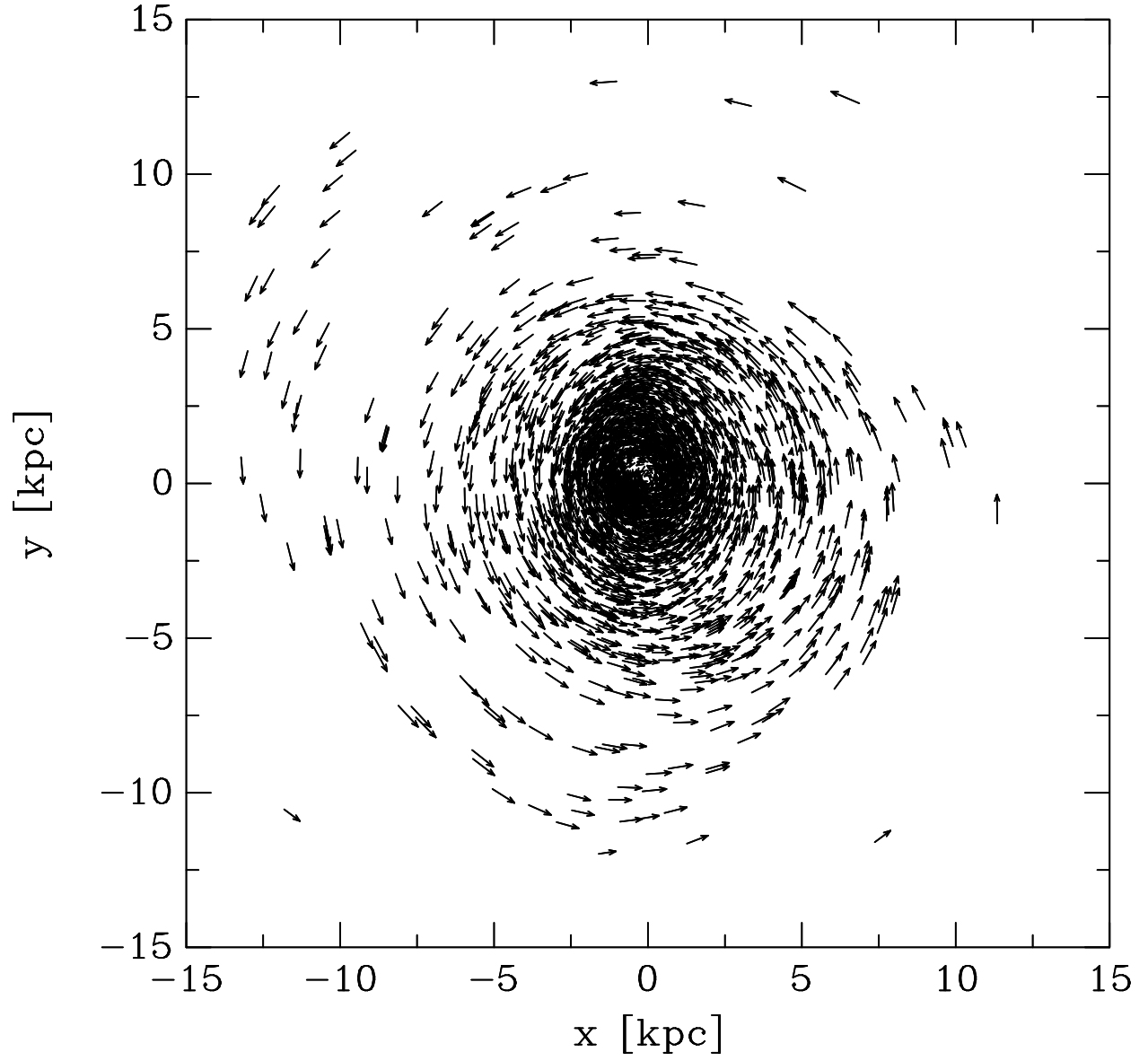


Fig. 7.— Face-on view of model galaxy $S4_{BO}$ at $z = 0$. Arrows represent the velocities of individual gas particles.

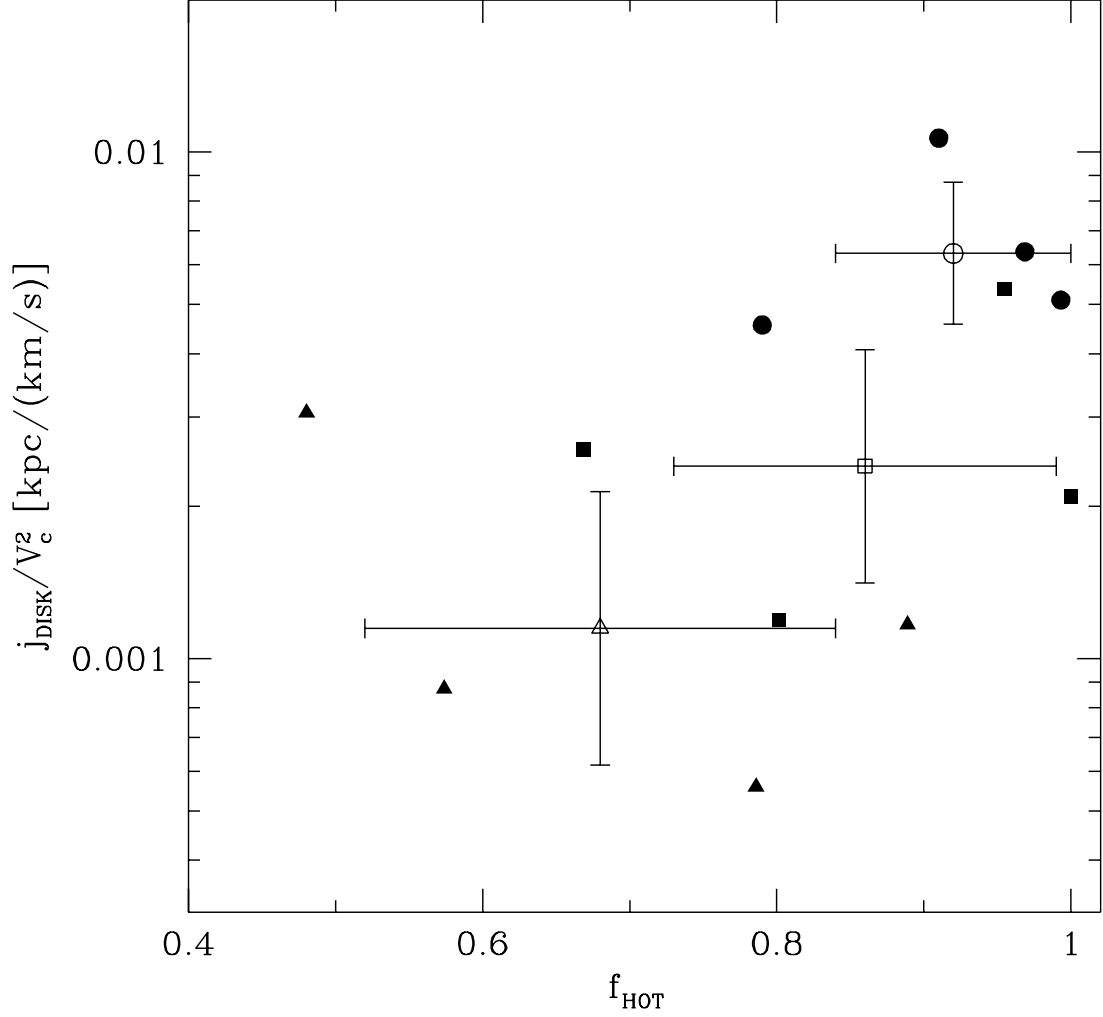


Fig. 8.— $\tilde{j}_{\text{disk}} \equiv j_{\text{disk}}/V_c^2$ versus the hot gas infall fraction f_{hot} for the simulations (symbols as in figure 1). The open symbols with error crosses represent the mean and standard deviation within each set of four simulations. There is no clear correlation between \tilde{j}_{disk} and f_{hot} within each set.

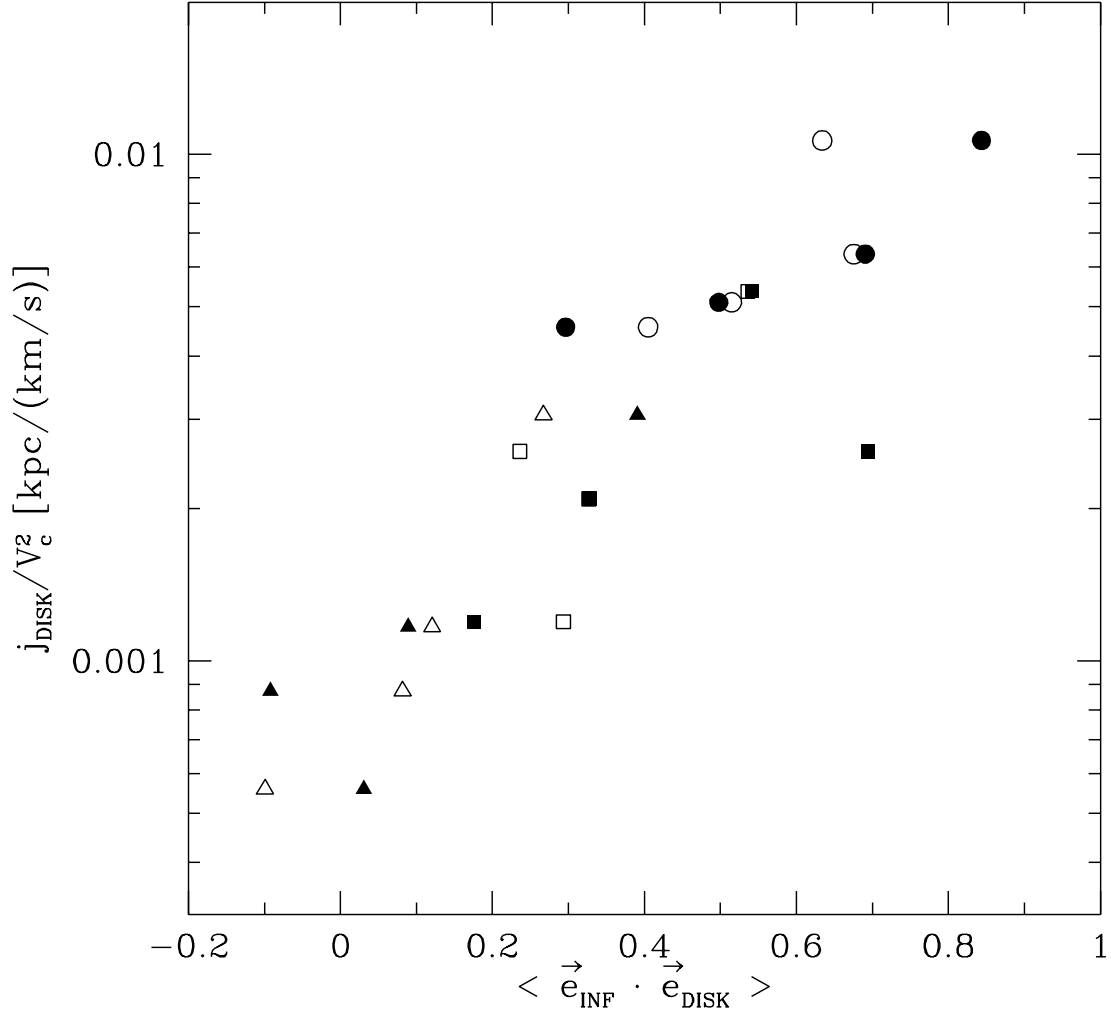


Fig. 9.— \tilde{j}_{disk} versus the mean cosine $\langle \vec{e}_{\text{inf}} \cdot \vec{e}_{\text{disk}} \rangle$ for the simulations. Filled symbols show results obtained by including only the hot gas in the definition of \vec{J}_{inf} . Open symbols show results obtained with all gas (hot and cold). Symbol shapes as in figure 1.

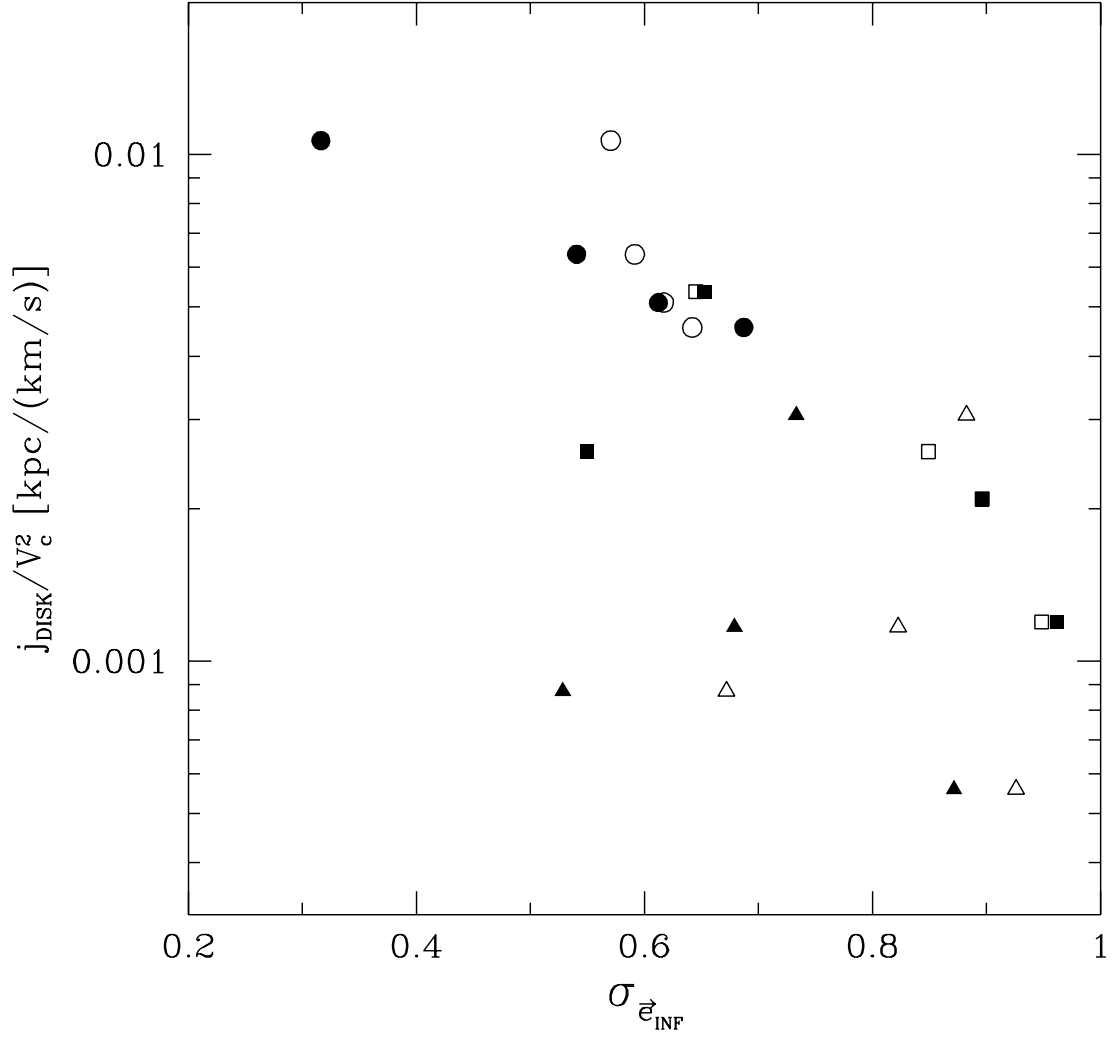


Fig. 10.— \tilde{j}_{disk} versus the dispersion in the cosines of figure 9. Symbols as in figure 9.

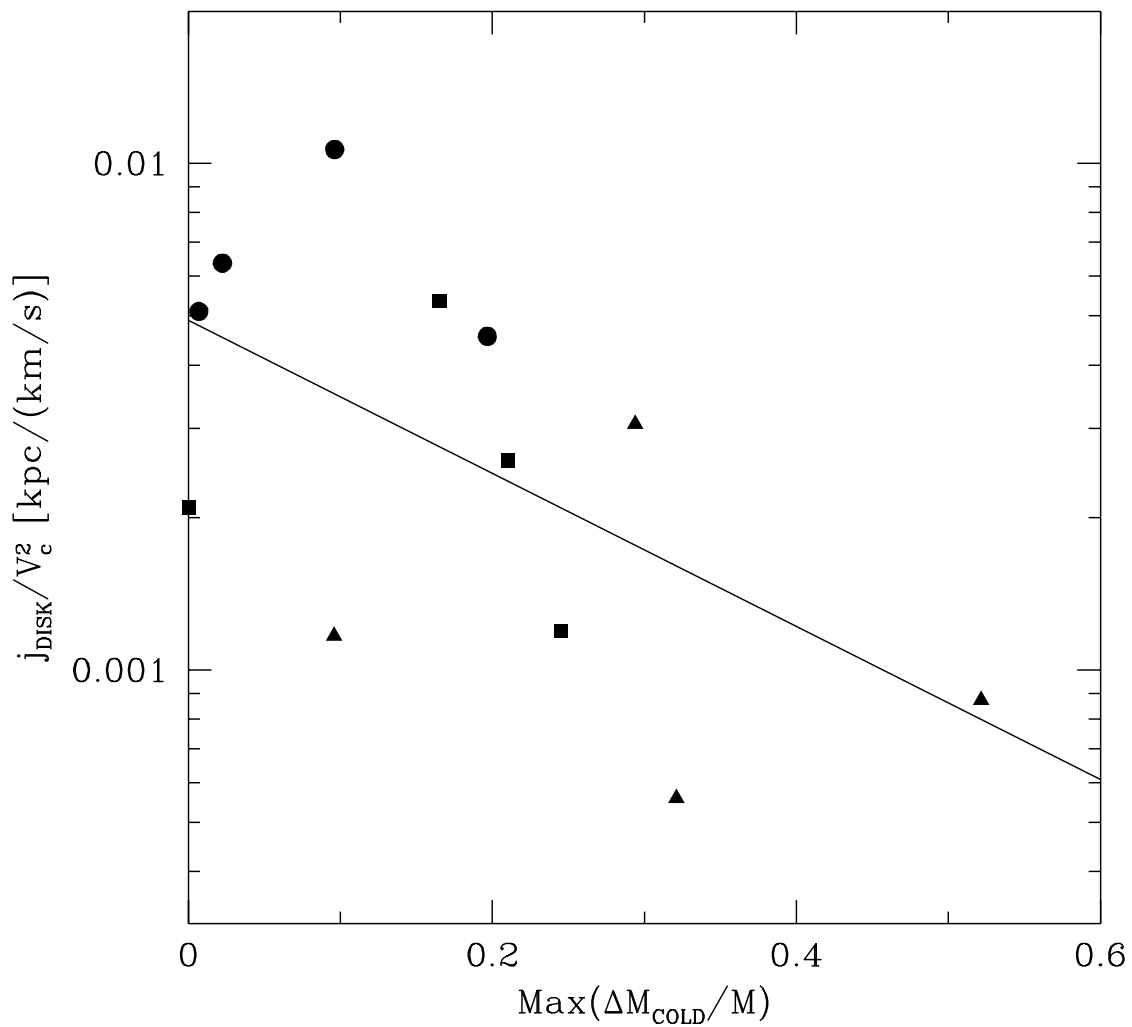


Fig. 11.— \tilde{j}_{disk} versus the maximum cold merger strength $\text{max}(\Delta M_{\text{cold}}/M)$ for the simulations. Symbols are as in figure 1. The solid line is a linear least squares fit.

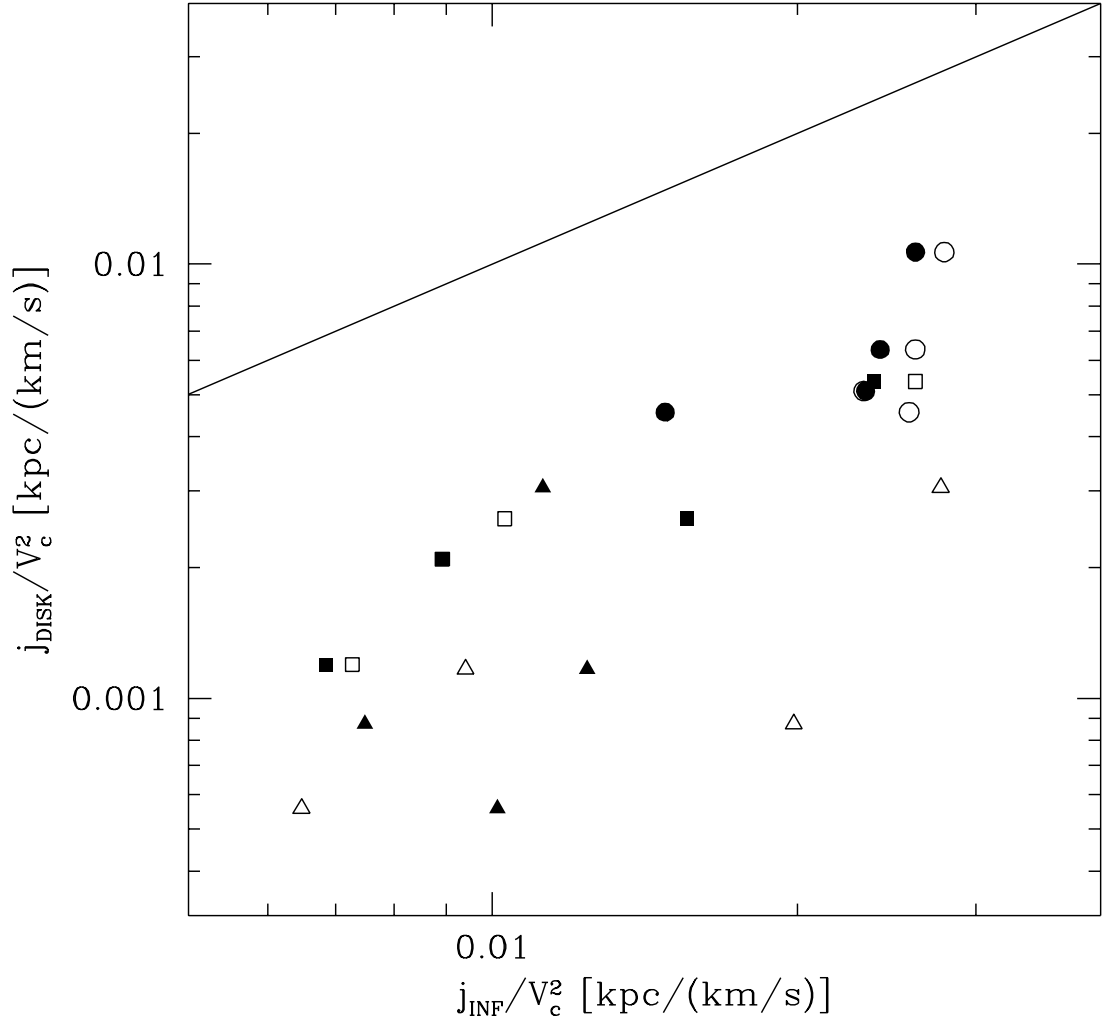


Fig. 12.— \tilde{j}_{disk} versus \tilde{j}_{inf} for the simulations. Symbols as in figure 9. The solid line corresponds to $\tilde{j}_{\text{disk}} = \tilde{j}_{\text{inf}}$.

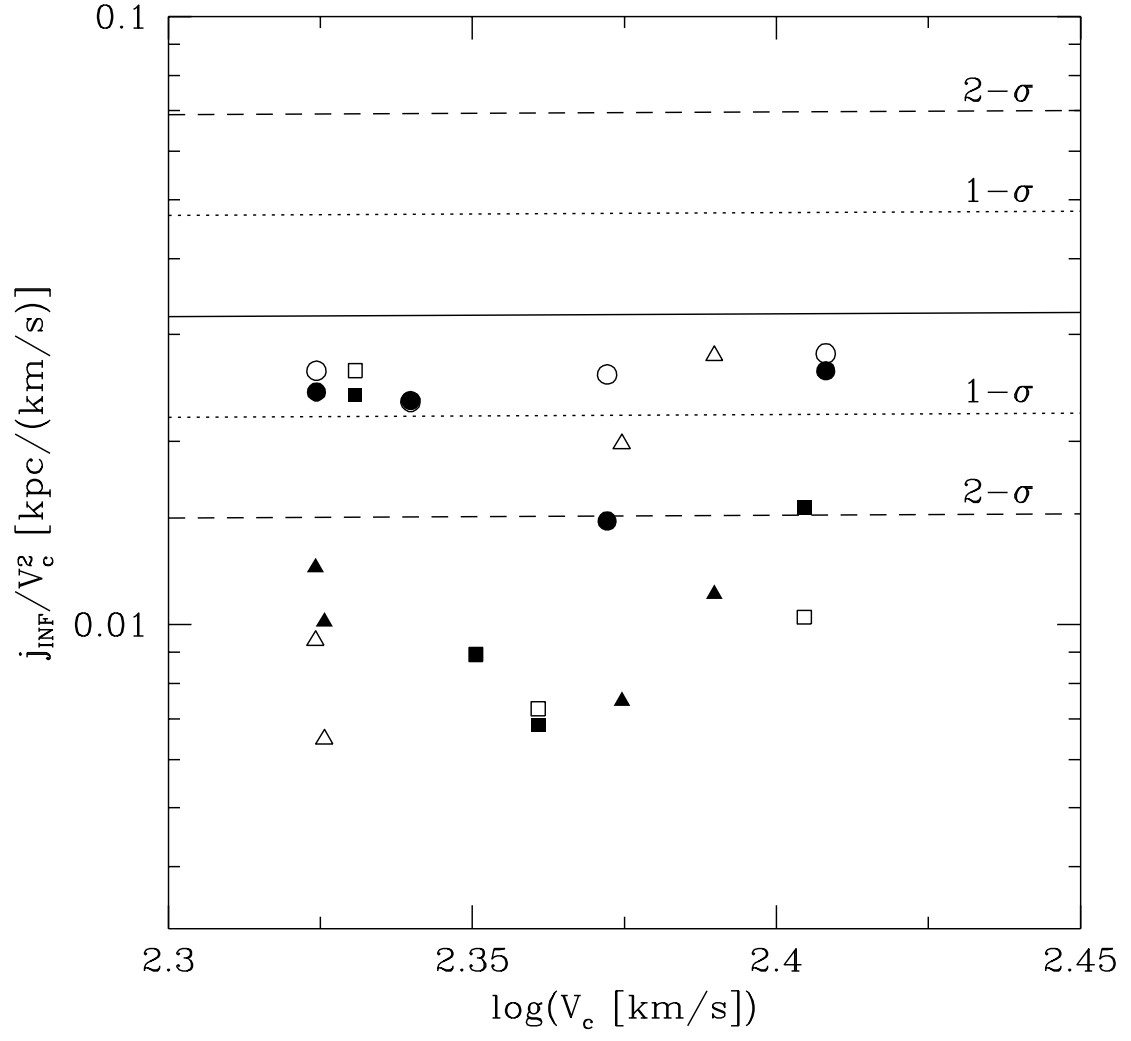


Fig. 13.— \tilde{j}_{inf} for the simulations. Symbols as in figure 9, horizontal lines as in figure 3.

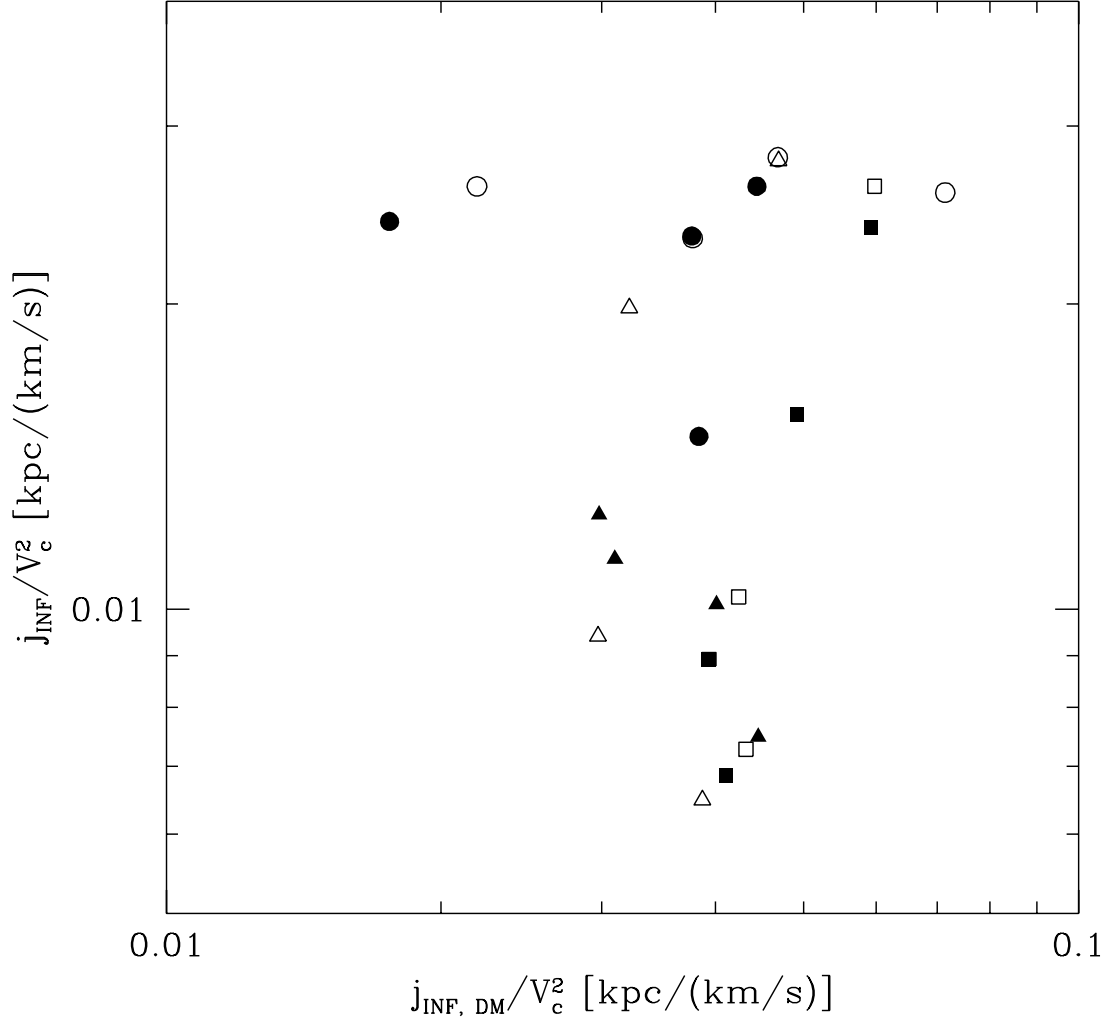


Fig. 14.— \tilde{j}_{inf} versus $\tilde{j}_{\text{inf,DM}}$ for the simulations. Symbols are as in figure 9.

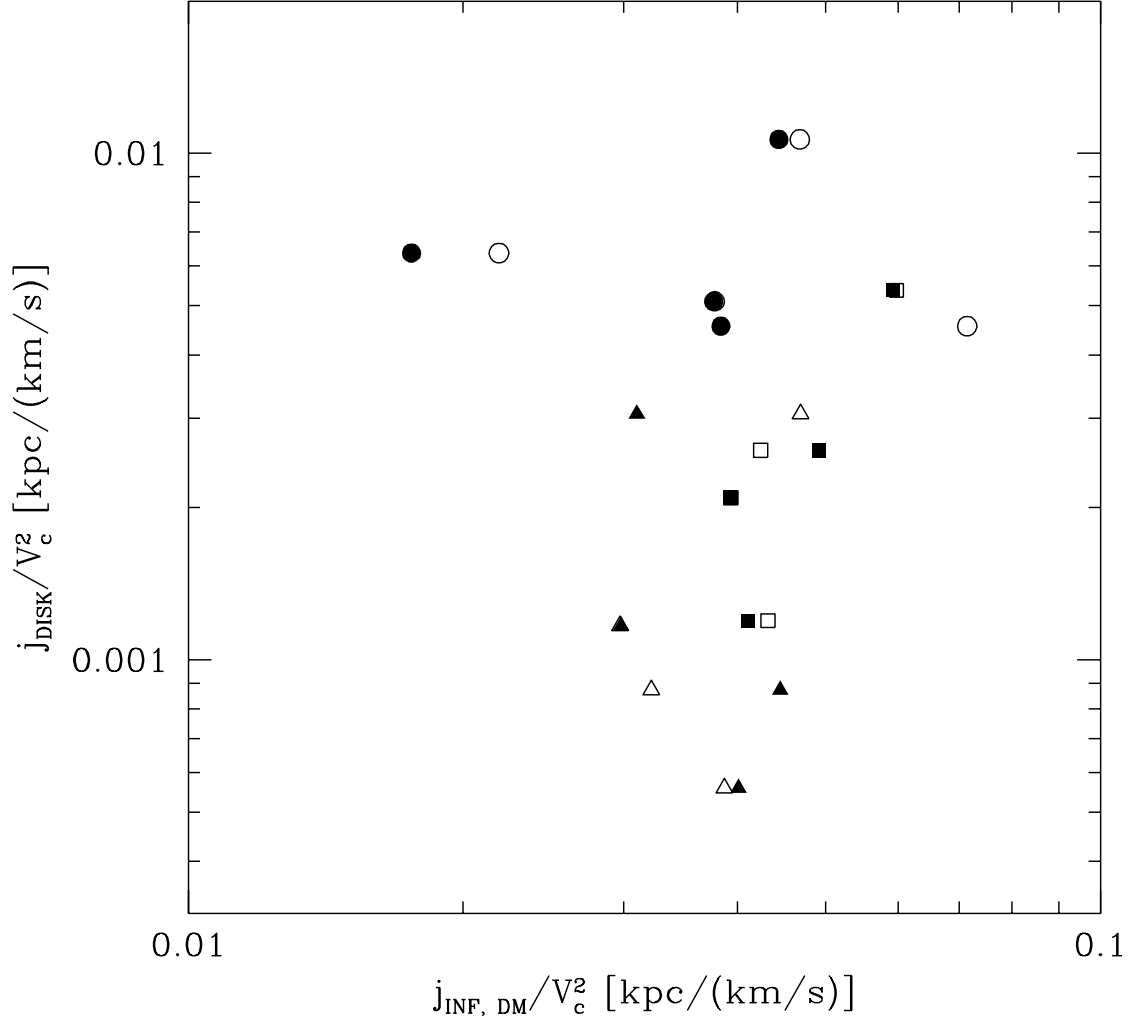


Fig. 15.— \tilde{j}_{disk} versus $\tilde{j}_{\text{inf,DM}}$ for the simulations. Symbols are as in figure 9.

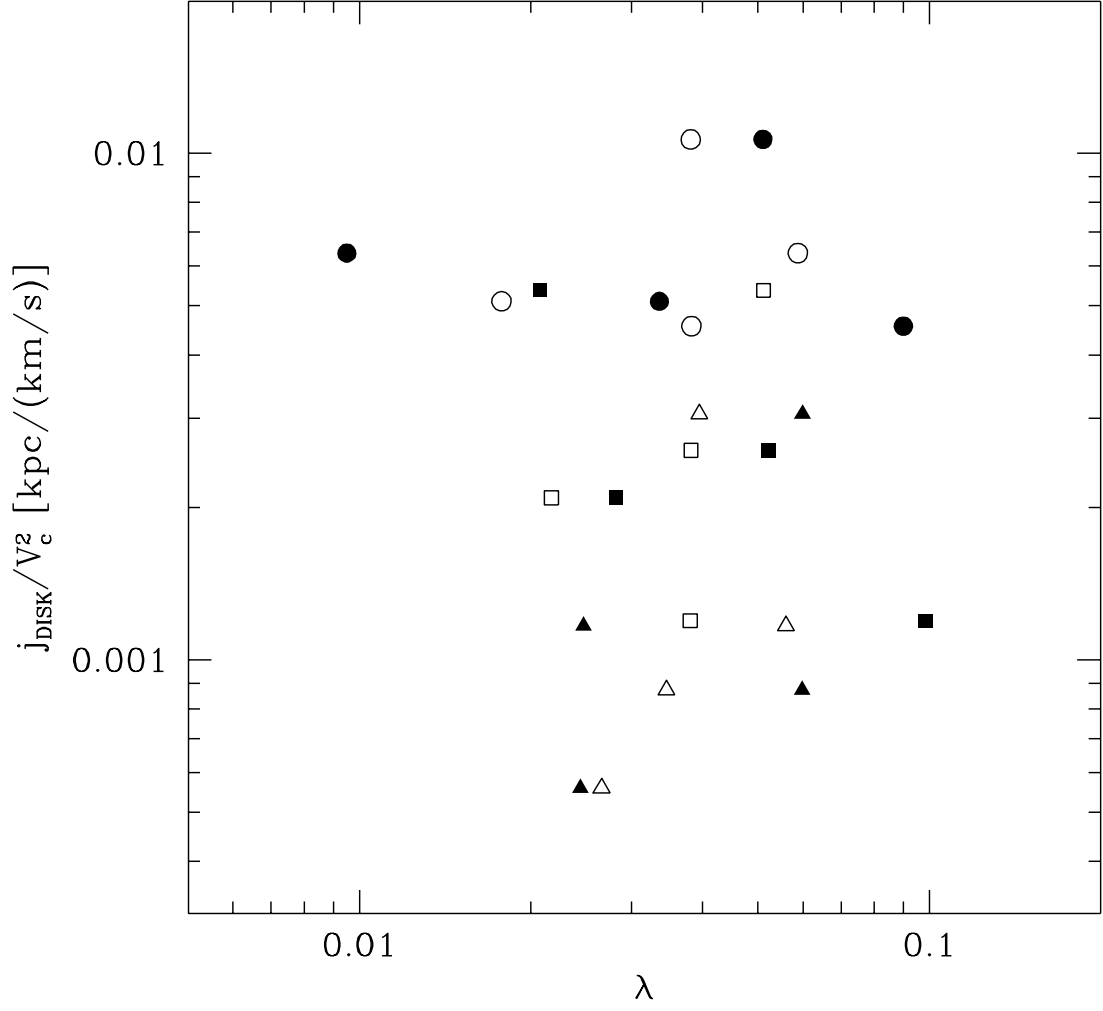


Fig. 16.— \tilde{j}_{disk} versus the spin parameter λ . Filled symbols are for λ evaluated at the baryonic infall radius r_{inf} , open symbols for λ evaluated at the virial radius r_{200} . Symbol shapes are as in figure 1.

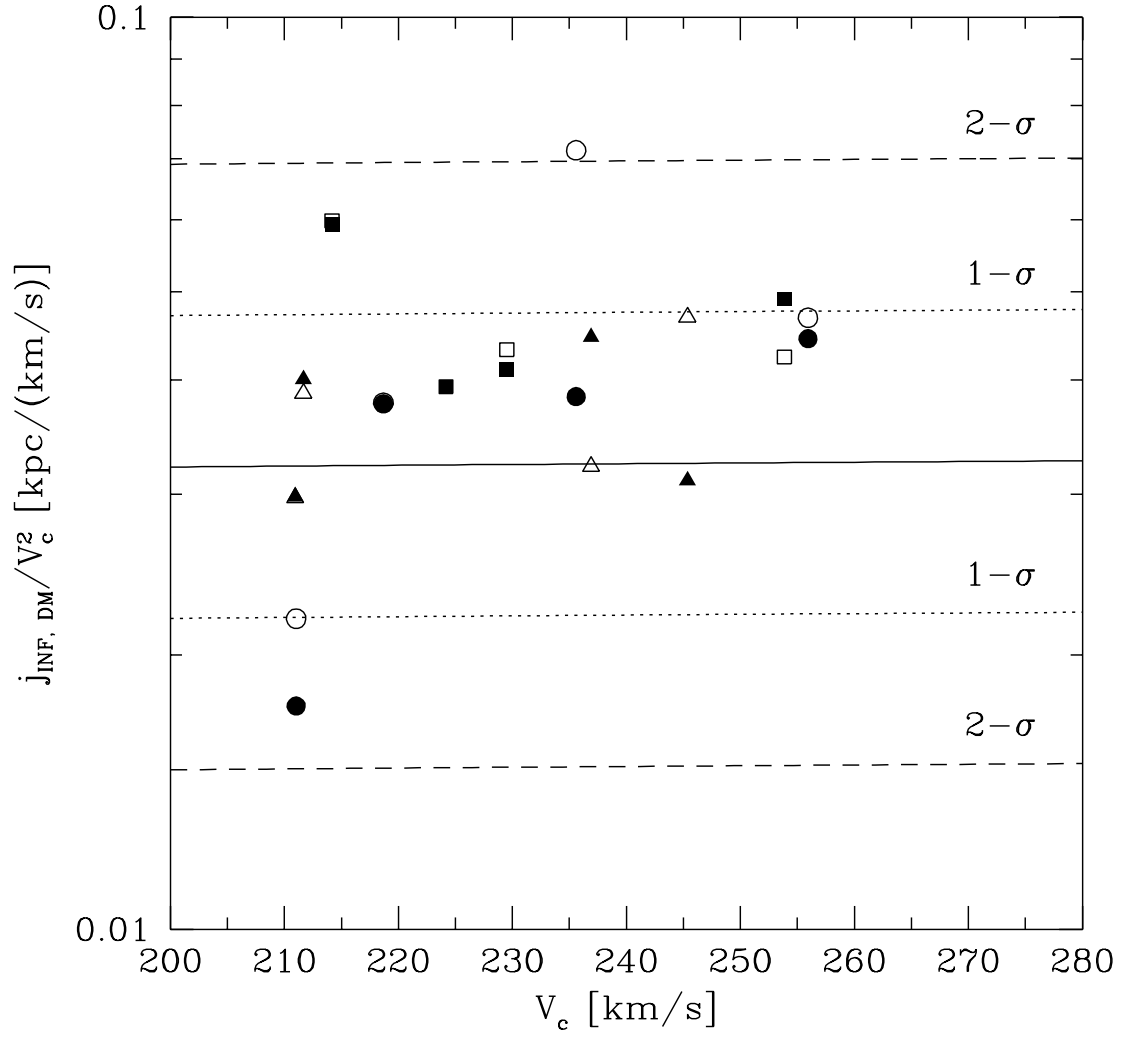


Fig. 17.— $\tilde{j}_{\text{inf, DM}}$ for the simulations. Symbols as in figure 9, lines as in figure 3.

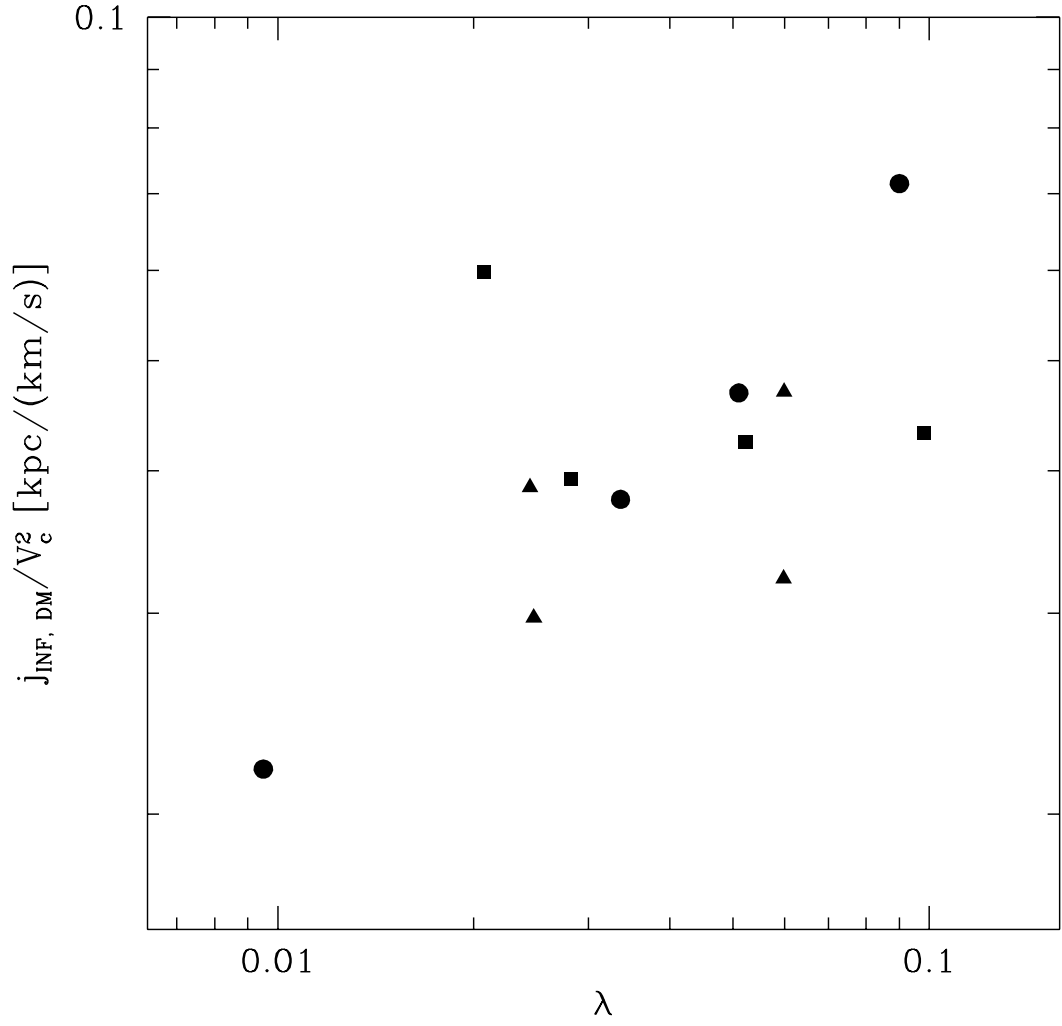


Fig. 18.— $\tilde{j}_{\text{inf, DM}}$ versus spin parameter $\lambda(r_{\text{inf}})$. Symbols as in figure 1.

Table 1: Particle counts in the high-resolution spheres

Label	N_{SPH}	N_{DM}
S1	13712	6856
S2	14170	7085
S3	14436	7218
S4	14726	7363

Table 2: Masses, sizes and velocities at $z = 0$

Label	M_{200} [$10^{12} \text{ M}_{\odot}$]	r_{200} [kpc]	V_{200} [km s^{-1}]	N_{gas}	N_{DM}	M_{gas} [$10^{10} \text{ M}_{\odot}$]	M_{DM} [$10^{12} \text{ M}_{\odot}$]	N_{disk}	M_{disk} [$10^{10} \text{ M}_{\odot}$]	M_{disk} [$\Omega_b M_{200}$]
S1 _{PA}	1.88	318	159	2937	1651	8.40	1.80	1574	4.50	0.48
S2 _{PA}	2.51	350	176	3922	2212	11.22	2.40	1566	4.48	0.36
S3 _{PA}	2.53	331	181	4285	2218	12.26	2.41	2273	6.50	0.51
S4 _{PA}	3.35	385	193	5418	2930	15.50	3.19	3260	9.33	0.56
S1 _{RH}	2.08	327	165	3416	1819	9.77	1.98	1521	4.35	0.42
S2 _{RH}	2.66	355	180	4276	2337	12.23	2.54	1665	4.76	0.36
S3 _{RH}	2.55	332	182	4232	2236	12.11	2.43	1774	5.08	0.40
S4 _{RH}	3.31	382	193	5310	2905	15.19	3.16	2896	8.29	0.50
S1 _{BO}	2.10	328	166	3303	1847	9.45	2.01	1818	5.20	0.49
S2 _{BO}	2.62	353	178	4038	2305	11.55	2.51	1606	4.59	0.35
S3 _{BO}	2.58	352	178	4202	2267	12.02	2.46	2190	6.27	0.48
S4 _{BO}	3.34	385	193	5017	2946	14.35	3.20	2219	6.35	0.38

Table 3: Angular momenta at $z = 0$

Label	V_c [km s ⁻¹]	b_{disk} [kpc]	λ	\dot{J}_{disk} [kpc km s ⁻¹]	r_{inf} [kpc]
S1 _{PA}	212	0.33	0.024	25	112
S2 _{PA}	211	0.38	0.025	52	83
S3 _{PA}	237	0.37	0.060	49	137
S4 _{PA}	252	0.54	0.060	184	138
S1 _{RH}	214	0.92	0.021	246	99
S2 _{RH}	224	0.72	0.028	105	98
S3 _{RH}	230	0.38	0.098	63	100
S4 _{RH}	254	0.54	0.049	167	123
S1 _{BO}	211	0.84	0.010	282	121
S2 _{BO}	219	0.80	0.034	243	94
S3 _{BO}	236	0.66	0.090	253	120
S4 _{BO}	256	2.25	0.051	698	87